RhoA mediates stress fiber strain site recognition by the LIM protein testin

Condensed title: RhoA drives testin to strained stress fibers

Stefano Sala and Patrick W. Oakes

Department of Cell and Molecular Physiology, Loyola University Chicago, Stritch School of Medicine, Maywood, IL 60153, USA

Corresponding author: Patrick W. Oakes

ORCID: 0000-0001-9951-1318

Email: poakes@luc.edu

Mailing address: Oakes Lab, Loyola University Chicago, Cell and Molecular Physiology Department, 2160 South First Avenue, CTRE Room 516, Maywood, Il 60153, USA

Abstract

The actin cytoskeleton is a key regulator of mechanical processes in cells. The family of LIM domain proteins have recently emerged as important mechanoresponsive cytoskeletal elements capable of sensing strain in the actin cytoskeleton. The mechanisms regulating this mechanosensitive behavior, however, remain poorly understood. Here we show that the LIM domain protein testin is peculiar in that despite the full-length protein primarily appearing diffuse in the cytoplasm, the C-terminal LIM domains alone recognize strained actin while the N-terminal domains alone recognize unstrained actin. Phosphorylation and cancer related mutations in the dimerization regions of testin, however, reveal its mechanosensitivity and cause it to relocate to focal adhesions and sites of strain in the actin cytoskeleton. Finally, we demonstrate activated RhoA causes WT testin to adorn stress fibers and become mechanosensitive. Together, our data show that testin's mechanoresponse is regulated in cells and provide new insights into LIM domain protein recognition of the actin cytoskeleton mechanical state.

Summary

LIM domain proteins recognize local strain in the actin cytoskeleton. This work suggests that the conformational state of the LIM protein testin determines its ability to recognize strained stress fibers and reveals a role for RhoA in regulating testin's mechanosensitivity.

Introduction

Cells depend on complex networks of both biochemical and mechanical signals which contribute to normal cellular physiology, tissue development and homeostasis (Lecuit et al., 2011; Iskratsch et al., 2014). While the general mechanisms of biochemical signaling are well defined, the mechanisms of mechanical signaling are less clear. Cells must recognize a variety of mechanical cues (e.g. tension, shape changes, pressure, stiffness), a behavior often referred to as mechanosensing, and convert those mechanical signals into biochemical signals, a process collectively called mechanotransduction (Paluch et al., 2015). These processes can influence a diverse array of critical functions including cell spreading (Oakes et al., 2018), force generation (Prager-Khoutorsky et al., 2011), proliferation (Rauskolb et al., 2014), migration (Das et al., 2015) and differentiation (Engler et al., 2006). Correspondingly, defects in mechanical signaling are associated with various diseases including muscular dystrophies and cardiomyopathies (Heydemann and McNally, 2007), osteoporosis (Hemmatian et al., 2017), asthma (Fabry and Fredberg, 2007), cancer progression and metastasis (Paszek et al., 2005).

The actin cytoskeleton and its associated binding proteins are key regulators of mechanical processes within and between cells (Ohashi et al., 2017; Blanchoin et al., 2014). Of the many diverse and dynamic architectures these proteins can form, two in particular play centralized roles in force transmission and mechanotransduction: focal adhesions (FA) and stress fibers (SF). FAs are complexes of ~150 proteins which couple the actin cytoskeleton to the extracellular environment, transmitting forces between the cell and the extracellular matrix (Kanchanawong et al., 2010; Zaidel-Bar et al., 2007). Those forces are generated primarily by non-muscle myosin II motors which pull on the actin filaments in SFs, propagating the force to the FAs where they terminate (Schwarz and Gardel, 2012; Oakes and Gardel, 2014). SFs themselves are composed of ~10-30 cross-linked actin filaments and can span tens of microns across the entire cell, providing an overall mechanical coherence to the cell (Tojkander et al., 2012; Cai and Sheetz, 2009; Svitkina, 2018).

As the combination of SFs and FAs serves as the primary conduit for force transmission in adherent cells, it is unsurprising that many proteins previously identified as mechanosensitive, such as alpha-actinin (Le et al., 2017), talin (Haining et al., 2016), vinculin (Goldmann, 2016), and integrins (Sun et al., 2016), are found in these structures. A common feature of these proteins is altered behavior under load, such as exposure of cryptic binding sites (Brown and Discher, 2009) or modified binding kinetics (Kong et al., 2009). An alternative and distinct mechanosensing mechanism, however, has been observed for the FA protein zyxin, which is induced to relocate to SFs under strain, whether through naturally occurring tears (Smith et al., 2011), optogenetically induced strain (Oakes et al., 2017) or when cells are placed under an externally applied cyclic stress (Hoffman et al., 2012; Yoshigi et al., 2005).

The family of proteins which are characterized by their LIM domains, consisting of two zinc-fingers, act as important scaffolds for protein-protein interactions (Smith et al., 2014; Sala and Ampe, 2018; Koch et al., 2012; Gill, 1995). Over the last two decades, many LIM domain-containing proteins (LDP) have, in addition to zyxin, been identified as mechanoresponsive cytoskeletal elements including paxillin (Smith et al., 2013), Hic-5 and CRP2 (Suzuki et al., 2005). More recently, it has been shown that several LDPs, including members of the zyxin, paxillin, Enigma and FHL families, share an evolutionarily conserved mechanism by which their LIM domains recognize mechanically strained F-actin (Sun et al., 2020; Winkelman et al., 2020). In all of these cases, their tandem LIM domains were necessary and sufficient for this mechanosensitive relocation. Remarkably, however, not all LDPs display mechanosensitive behavior and the mechanoresponse is not identical amongst LDPs. For instance, both zyxin and paxillin recognize SF strain sites (SFSS) but only zyxin relocates to SFs in response to cyclical stretch (Smith et al., 2013; Suzuki et al., 2005). This implies that LIM domain protein mechanosensitivity is specific and regulated. Dissecting these LDP-specific mechanosensitivity mechanisms and how they are regulated is necessary to better understand the molecular mechanisms underlying cellular mechanoresponse.

To probe this topic further, we investigated the mechanosensitivity of the multimodular LDP testin. Testin is expressed in the majority of tissues and consists of an N-terminal CR (Cysteine-rich), central PET (Prickle, Espinas, Testin) and three C-terminal LIM (Lin-11, Isl-1, Mec-3) domains (Boëda et al., 2011; Sala et al., 2017a; Tobias et al., 2001). While the exact function of testin remains ill-defined, reduced expression has been observed in various tumors and cancer cell lines which, in conjunction with a number of animal studies, suggests a tumor suppressor function (Sarti et al., 2005; Drusco et al., 2005; Zhu et al., 2012; Gu et al., 2014). Patient tumor samples have also revealed the existence of several cancer-associated mutations in the TES gene (Tatarelli et al., 2000; Ma et al., 2010; Weeks et al., 2016; portal.gdc.cancer.gov). Both the functional consequences of these mutations as well as the molecular mechanisms underlying its tumor suppressor function remain elusive. While testin has primarily been associated with the actin cytoskeleton, a proteomics-based interactome study additionally identified over putative 100 testin binding partners in a domain-specific manner, linking testin to adhesions, microtubules, endocytosis and nuclear receptor-mediated transcription among others (Sala et al., 2017b), illustrating testin’s likely multifunctional nature. Truncation variants consisting of either the N-terminal CR and PET domains or C-terminal LIM domains, have been shown to localize to SFs and FAs, respectively (Garvalov et al., 2003; Sala et al., 2017b). In contrast, full-length testin is mainly distributed in the cytoplasm, consistent with its multi-conformational nature (Garvalov et al., 2003; Sala et al., 2017a). Together these findings suggest that the regulation of testin's activity, and thus its mechanosensitivity, is likely mediated by its conformational state. We therefore hypothesized that testin is mechanosensitive under certain conditions and exploited its modular nature to investigate its potential role in recognizing local strain in the actin cytoskeleton.

Here we show testin is unique in that it contains separate domains which preferentially recognize strained and unstrained filamentous actin, and yet the full-length protein primarily resides in the cytoplasm. Specifically, the C-terminal LIM domains of testin relocate to SFSSs, for which a single LIM domain is sufficient, while the N-terminal domains only recognize unstrained SFs. Phosphorylation and cancer related point mutations in the dimerization regions induce testin to relocate to both FAs and to SFSSs suggesting its mechanosensitivity is regulated. Finally, we show that testin relocates from the cytoplasm to SFs and SFSSs in the presence of active RhoA, suggesting a possible role of RhoA in regulating testin's mechanosensitivity. Together, our findings reveal an important context-specific function for testin in recognizing SF strain and provide new insights into the general regulation of LDP mechanosensitivity in the actin cytoskeleton.

Results

The LIM domains of testin, but not the full-length protein, recognize stress fiber strain sites

A subset of LIM domain proteins, including members of the FHL, zyxin and paxillin families, are known to recognize SFSSs via their LIM domains (Smith et al., 2011; Sun et al., 2020; Winkelman et al., 2020). To investigate whether the LIM domains of testin (LIM 1-2-3, Fig. 1A) display a similar mechanosensitive behavior, we engineered a series of truncations fused to GFP and co-expressed them with mApple-actin in human foreskin fibroblasts (HFF). LIM 1-2-3 localizes to FAs as previously reported (Fig. 1A, (Garvalov et al., 2003)). We then used a laser photoablation system to locally induce a SFSS, marked by a recoil and thinning of the SF (Fig. 1B, (Smith et al., 2011)). Potential recruitment was monitored by tracking the GFP signal over time using a mask based on the brightest pixels in the region surrounding the ablation that increased the most in intensity compared to their pre-ablation state (Figs. 1B,C, S1). The same pixels were then used to monitor the intensity of actin in those regions. Following photoablation, we observed a rapid increase in the GFP signal within seconds as LIM 1-2-3 relocated to the induced SFSS and a concomitant loss of actin intensity as the SF was damaged (Fig. 1B,C, Movie S1). Following LIM 1-2-3 recruitment, the actin signal subsequently recovered within minutes, indicating SF repair (Smith et al., 2011), before it finally plateaued.

To assess the spatial distribution of the LIM 1-2-3 localization, we aligned the masks to the angle of ablation, summed each experimental group over time, and averaged them to create a spatial probability map (Fig. S1D). This map clearly shows the brightest LIM 1-2-3 signal is located in the center of the mask stack where the ablation occurred (red line, Fig. 1C) and where the region of strain is located (dashed circle, Fig. 1C). To confirm that this is a SFSS, we assessed relocation of LIM 1-2-3 in the presence of mCherry-conjugated zyxin, a known SF strain sensor (Smith et al., 2011), and used SiR-Actin to visualize the SFs. Masks in these experiments were created based on regions where zyxin increased in intensity. Immediately following strain induction, both zyxin and LIM 1-2-3 relocated to and colocalized at SFs with similar kinetics, confirming the LIM domains of testin recognize actual SFSSs (Fig. 1D, Movie S2).

In contrast to its LIM domains, full-length (FL) testin is mainly cytoplasmic with only a small subpopulation localizing to FAs (Fig. 1E). When a SFSS was induced, we did not observe recruitment of FL testin (Fig. 1F,G, Movie S1) and instead saw a rapid recovery of fluorescence intensity consistent with diffusion. Correspondingly, the spatial probability of recruitment map shows a random distribution and no regions of local enrichment in the central region of strain (Fig. 1G). When this experiment was repeated using zyxin as a control, we observed a rapid relocation of zyxin, but not testin, to sites of strain. This confirms that in our steady-state conditions FL testin is unable to recognize SFSSs (Fig. 1H, Movie S2).

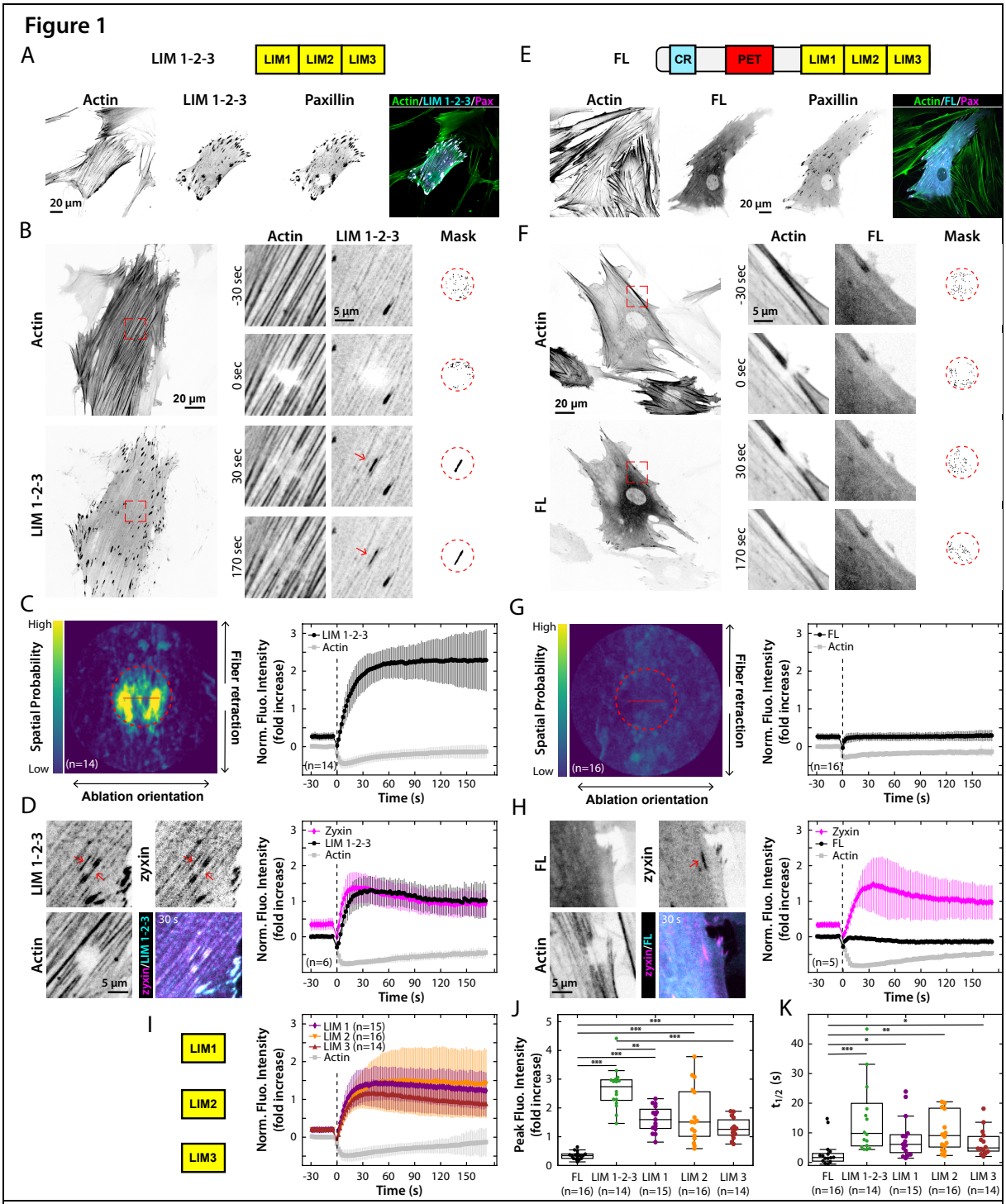

Figure 1: The LIM domains of testin, but not full-length, recognize stress fiber strain sites
A,E) Domain organization and subcellular localization of the LIM domains of testin (LIM 1-2-3) and full-length testin (FL) in HFFs. GFP-LIM 1-2-3 localizes strongly to FAs (A) whereas GFP-FL displays a diffuse cytoplasmic and weak FA localization (E). GFP-testin, mApple-paxillin and SiR-Actin channels are shown. **B,F)** HFFs co-expressing mApple-actin and either GFP-LIM 1-2-3 (B) or GFP-FL testin (F). Magnified inset images (red boxed regions) display the localization of each construct during the timelapse. Red arrows indicate relocation of LIM 1-2-3 to SFSSs (Movie S1). Masks show the pixels in the region surrounding the ablation (red dashed circle) that increased the most in intensity compared to their pre-ablation state. **C,G)** Spatial probability of testin recruitment (left) and average fluorescence intensity traces with standard deviation of the testin and actin signals (right) in the region of strain. The brightest LIM 1-2-3 signal is located in the central region of strain (C, dashed circle) whereas the brightest FL signal is distributed randomly (G). Red line represents the 5 µm laser line used to photo-induce SFSSs. Following SFSS induction, a rapid and large increase of the LIM 1-2-3 signal (C) but no change of the FL testin signal was detected in

the region of strain (G). **D,H)** Experiments shown in C and G were repeated in the presence of the SFSS marker mCherry-zyxin, and SiR-Actin (Movie S2). Increased LIM 1-2-3 fluorescence intensity in the region of strain and colocalization with zyxin at SFSSs (D, red arrows). FL signal remained unchanged after ablation and did not colocalize with zyxin (H). **I)** Average fluorescence intensity traces and standard deviation of testin's individual GFP-coupled LIM domains and mApple-actin signals in the region of strain indicating recruitment to SFSSs of each LIM domain. **J)** Distribution of the peak fluorescence intensities after SFSS induction per testin variant. **I)** Recruitment $T_{1/2}$ after SFSS induction per testin variant. *: $p \leq 0.05$., **: $p \leq 0.01$, ***: $p \leq 0.001$. Dashed vertical lines in C, D, E, H and I indicate the ablation timepoint.

A single LIM domain is sufficient to recognize SFSSs

To further dissect the mechanoresponsive regions within testin's LIM domains, we investigated the ability of the individual LIM domains (LIM 1, LIM 2 and LIM 3; Fig. 1I) to recognize SFSSs. Previous research has suggested that multiple LIM domains are required for mechanosensitivity (Sun et al., 2020; Winkelman et al., 2020). Surprisingly, not only did each LIM domain of testin display FA localization, they also relocated to SFSSs (Figs. 1I,1J, S2; Movie S3). In order to compare the recruitment magnitude and kinetics to SFSSs of testin's LIM domains, we fit an exponential recovery curve to the average traces of the various constructs (Fig. S3) and calculated the $t_{1/2}$, amplitude and plateau maximum of the exponential fit (Fig. 1K;Table 1). Based on these values, the recruitment kinetics of LIM 1-2-3 are very similar to those of the individual LIM domains. Of the individual LIM domains, LIM 2 showed the greatest recruitment, though this recruitment remained slightly less than LIM 1-2-3 (Table S1, Fig. 1J,H). These data illustrate that each of testin's LIM domains recognize SFSSs and that their mechanosensitivity is blocked in the full-length protein.

The N-terminal and C-terminal halves of testin recognize different mechanical states of F-actin

We next tested whether the N-terminal half of testin (NT), containing the CR and PET domains (Fig. 2A), is capable of recognizing SFSSs. Despite an initial strong SF localization (Fig. 2A), we did not observe any obvious enrichment of NT at SFSSs (Fig. 2B,C; Movie S1). However, quantification of the fluorescence intensity in the masked region of strain did reveal a slight increase of the NT signal (Fig. 2D,E). Upon closer examination we noticed that the actin signal also increased in these regions, opposite to what is expected for a SFSS (Fig. 2D). Examination of the spatial distribution of the recruitment revealed that the brightest NT signal was located outside of the central region of strain along the recoil axis of the actin (Fig. 2C) and was smaller in magnitude than the LIM 1-2-3 signal (Fig. 2E). Together these data indicate that, unlike LIM 1-2-3, the increase in fluorescence of NT arises from a condensation of severed actin filaments and not from additional recruitment (Fig. 2C,D). Therefore, in contrast to its LIM domains, the N-terminal half of testin is unable to bind SFSSs and instead only associates with unstrained SFs.

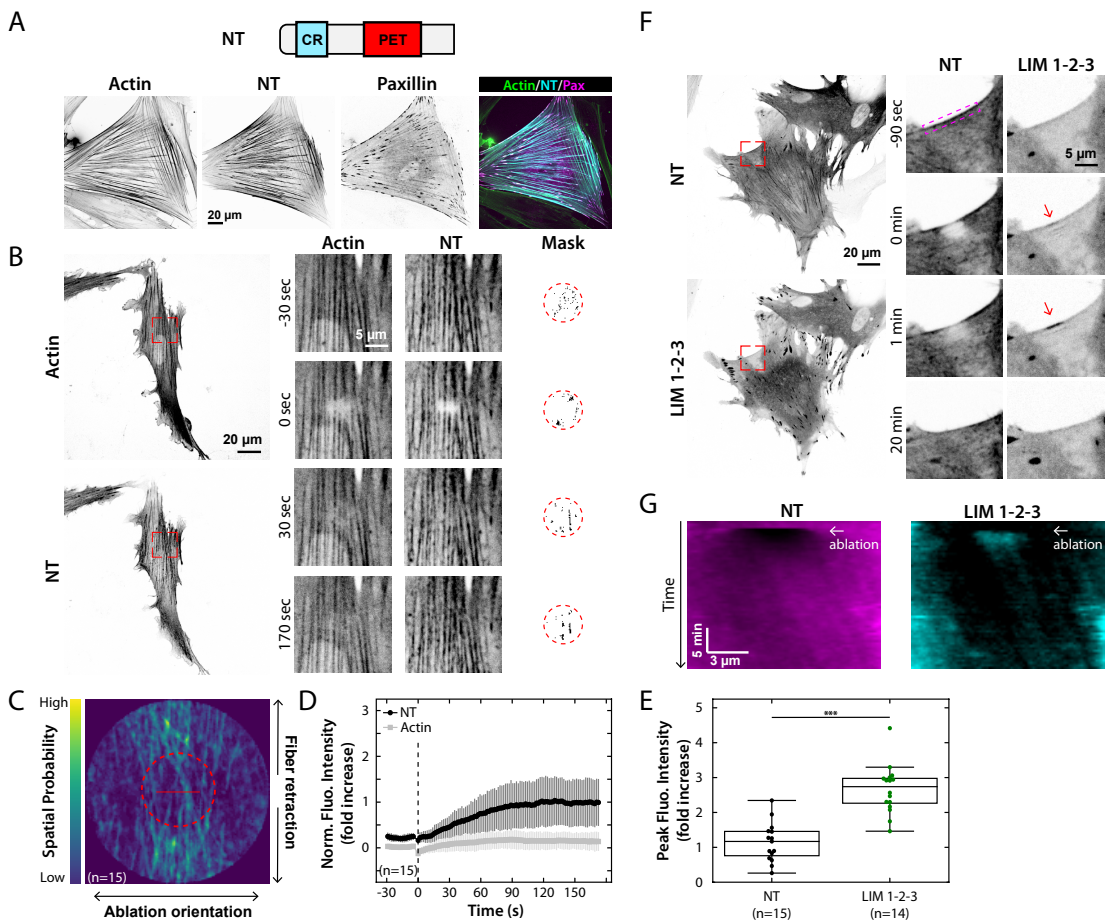

Figure 2: The N-terminal domains and C-terminal LIM domains of testin recognize different mechanical states of SFs

A) Domain composition and subcellular localization of the N-terminal domains of testin (NT). GFP-NT localizes strongly to SFs. GFP-NT, mApple-paxillin and SiR-Actin channels are shown. **B)** HFFs co-expressing mApple-actin and GFP-NT. Magnified inset images (red boxed regions) display the localization of NT during the timelapse (Movie S1). Masks show the pixels in the region surrounding the ablation (red dashed circle) that increased the most in intensity compared to their pre-ablation state. **C)** Spatial probability of NT recruitment in the region of strain shows NT is primarily recruited outside the central region of strain (red dashed circle). Red line represents the 5 µm laser line used to photo-induce SFSSs. **D)** Average fluorescence intensity trace and standard deviation of the NT and actin signals in the region of strain. Dashed vertical line indicates the ablation timepoint. **E)** Distribution of the peak fluorescence intensities after SFSS induction for NT and LIM 1-2-3. ***: $p \leq 0.001$. **F)** HFFs co-expressing GFP-LIM 1-2-3 and mApple-NT. Magnified inset images (red boxed regions) display the localization of each construct during timelapse showing recruitment of GFP-LIM 1-2-3 to SFSSs (red arrows) and absence of colocalization of GFP-LIM 1-2-3 and mApple-NT (Movie S4). **G)** Kymograph along the magenta boxed SF in F showing recruitment of LIM-1-2-3 to the SFSS following ablation and simultaneous dissociation of NT in the same region. Arrows indicate the ablation timepoint

To further illustrate this, we co-expressed LIM 1-2-3 and NT and assessed whether the two halves of testin colocalized at all following induction of a SFSS (Fig. 2F, Movie S4). To ensure full repair of the ablated SF, we monitored their localization over a time period of 30 min (Fig. 2F,G). Prior to SFSS induction, LIM 1-2-3 localized to FAs whereas NT localized to SFs as mentioned above (Fig. 2F,G). After SFSS induction, LIM 1-2-3 was immediately recruited to the strain site (arrows, Fig. 2F,G)

while NT simultaneously dissociated from the strain region (Fig. 2F,G). NT remained bound to SFs in the regions flanking the strain site. As the SFSS was repaired over time, LIM 1-2-3 dissociated from the ablated SF and NT reassociated with the repaired actin fibers (Fig. 2F,G). The absence of colocalization of NT and LIM 1-2-3 at either unstrained or strained SF sites demonstrates that the two halves of testin recognize different mechanical states of F-actin.

The LIM domains of testin recognize strained, but not severed, SFs

To verify that laser-induced damage actually results in the induction of a SFSSs, we combined our laser photoablation approach with traction force microscopy. Visualizing LIM 1-2-3 and actin during an ablation, we simultaneously measured the traction stresses at the FAs that were connected to the photodamaged SFs (Fig. 3A, Movie S5). As expected, we observed a rapid relocation of LIM 1-2-3 to the strain region following ablation (Fig. 3A-C). Subtle changes in the traction stresses were localized at the ends of the damaged SFs and were concomitant with the ablation (Fig. 3D). We saw, however, only a minor reduction in the total contractility of the cell (Fig. 3B). Together, these results indicate that the SFs remain under tension following damage from our photoablation system and are not fully severed.

Previous work has demonstrated the presence of free barbed ends in naturally occurring spontaneous SFSSs (Smith et al., 2011). This raises the possibility that the LIM domains of testin associate with these barbed ends in SFSSs in addition to recognizing strained actin fibers. To test this, we increased the local laser power to completely sever SF bundles and assessed whether testin's LIM domains recognized free actin filament ends in the absence of strain. Fig. 3E shows two SFs arranged in a Y-shape (red box), where the bottom fiber is completely severed, confirmed by the complete loss of the actin signal, and the top fiber becomes strained. Recruitment of LIM 1-2-3 only occurred on the strained fiber, and not along the retracting fiber with the free ends (Fig. 3E, Movie S6). This supports that testin's LIM domains do not recognize barbed actin filament ends.

Recruitment of testin's LIM domains to strained actin is independent of zyxin

The LDP zyxin can directly interact with the first LIM domain of testin (Hadzic et al., 2015). Therefore, the observation that the LIM domains of testin colocalize with zyxin at SFSSs (Fig. 1D) raises the possibility that zyxin is responsible for recruiting testin to those strain sites. To investigate this, we overexpressed LIM 1-2-3 in a zyxin knockout mouse embryonic fibroblast line (zyxin$^{(-/-)}$ MEFs, (Hoffman et al., 2006)). Western blot analysis confirmed that the cells lacked zyxin (Fig. 3F). Consistent with our previous results, we observed strong relocation of LIM 1-2-3 to SFSSs in zyxin$^{(-/-)}$ MEFs (Fig. 3G,H; Movie S7). These results indicate that the LIM domains of testin recognize SFSSs in a zyxin-independent manner.

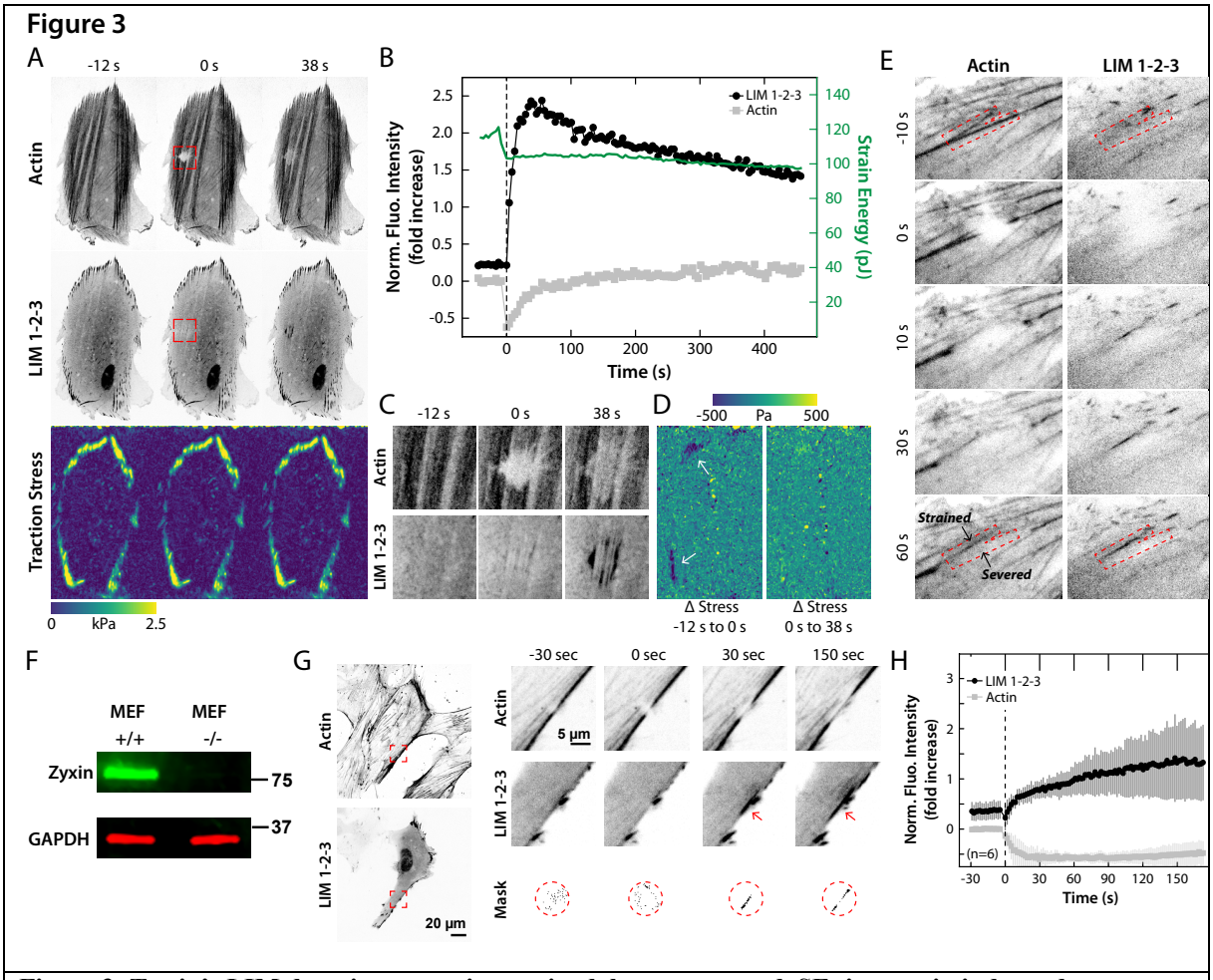

Figure 3: Testin's LIM domains recognize strained, but not severed, SFs in a zyxin independent manner.
A) HFFs expressing mApple-actin and GFP-LIM 1-2-3 and the corresponding traction stresses. **B)** Simultaneous measurements of the total cellular strain energy and relative zyxin and actin intensities at the site of strain indicate the ablated SFs remain under tension. **C)** Magnified inset images (red boxes in **A**) display the localization of each construct during the timelapse (Movie S5). **D)** Difference in traction stresses pre-ablation and post-ablation show that traction stresses are reduced at the ends of the SFs (white arrows) that are damaged during ablation. **E)** HFFs expressing mApple-actin and GFP-LIM 1-2-3 during ablation of Y-shaped SFs are shown (red dashed box). LIM 1-2-3 relocates to the strained SF but not the severed SF (Movie S6). **F)** Western blot analysis of WT (MEF +/+) and zyxin KO (MEF -/-) MEF lysates showing no detectable zyxin levels in the zyxin$^{(-/-)}$ MEFs. **G)** GFP-LIM 1-2-3 expressing zyxin$^{(-/-)}$ MEFs stained with SiR-Actin. Magnified inset images (red boxed regions) display the localization of LIM 1-2-3 and actin signal during timelapse showing recruitment of LIM 1-2-3 to SFSSs (red arrows, Movie S7). Masks show the pixels in the region surrounding the ablation (red dashed circle) that increased the most in intensity compared to their pre-ablation state. **H)** Average fluorescence intensity trace and standard deviation of the LIM 1-2-3 and actin signals in the region of strain. Dashed vertical line indicates the ablation timepoint.

Tyrosine mutations in the PET and LIM 1 domains drive testin to SFSSs

Given the multi-conformational nature of testin (Sala et al., 2017a; Garvalov et al., 2003), it is possible that the inability of FL testin to recognize SFSSs results from a conformational state that makes the LIM domains inaccessible. Previous work demonstrated that tyrosine 288 (Y288) in the first LIM domain is structurally important for testin dimerization since mutating this tyrosine to alanine strongly

inhibits dimerization (Sala et al., 2017a). Therefore, we hypothesized that mutating Y288 to alanine would allow testin to recognize strain in the actin cytoskeleton by adopting a more favorable conformation.

To investigate this, we co-expressed a GFP-Y288A mutant of testin (Y288A; Fig. 4A) along with actin in HFFs and assessed its ability to relocate to SFSSs (Movie S8). Induction of SFSSs resulted in a moderate but obvious recruitment of Y288A to the site of strain (Fig. 4A). The spatial probability map also revealed a preference for recruitment in the region of strain (Fig. 4B). To further investigate the potential regulatory role of Y288 in determining testin's mechanosensitivity, we created a phosphomimetic glutamic acid (Y288E) and non-phosphorylatable phenylalanine (Y288F) mutants of testin and assessed their ability to recognize SFSSs (Fig. 4C,D,E,F; Movie S8). Similar to Y288A, Y288E was capable of recognizing SFSSs (Fig. 4C,D,G,H). Conversely, the Y288F mutants did not display this mechanosensitive behavior (Fig. 4E-H). These data illustrate that specific mutations of Y288 in the first LIM domain can promote testin's mechanosensitivity.

Testin forms dimers through an interaction between an N-terminal region containing the PET domain and the first two C-terminal LIM domains (Sala et al., 2017a). Since Y288 is located in the C-terminal dimerization region of testin (LIM 1), we reasoned that other tyrosines in the N-terminal dimerization region might similarly affect testin's mechanosensitivity. We therefore investigated tyrosine 111 (Y111), located in the N-terminal PET domain, by creating non-phosphorylatable alanine (Y111A) and phenylalanine (Y111F) mutants as well as a phosphomimetic glutamic acid (Y111E) mutant (Fig. 5A,B,C,D,E,F; Movie S8). Interestingly, we observed a similar behavior for the Y111 mutants with clear recruitment of Y111A (Fig. 5A,G-H) and Y111E (Fig. 5C,G-H) mutants to SFSSs but not the Y111F mutant (Fig. 5E,G-H). Our quantitative analysis further revealed that the relocation of the Y111A and Y111E mutants to sites of strain (Fig. 5G-H) was stronger than what we observed for the corresponding mechanosensitive Y288 mutants (Fig. 4G-H), suggesting these mutants recognize SFSSs with different affinities (Fig. S3;Table 1). These results demonstrate that mutations in the dimerization regions of testin affect its ability to recognize strain in the actin cytoskeleton, and that the magnitude of the effect is dependent on the specific residue.

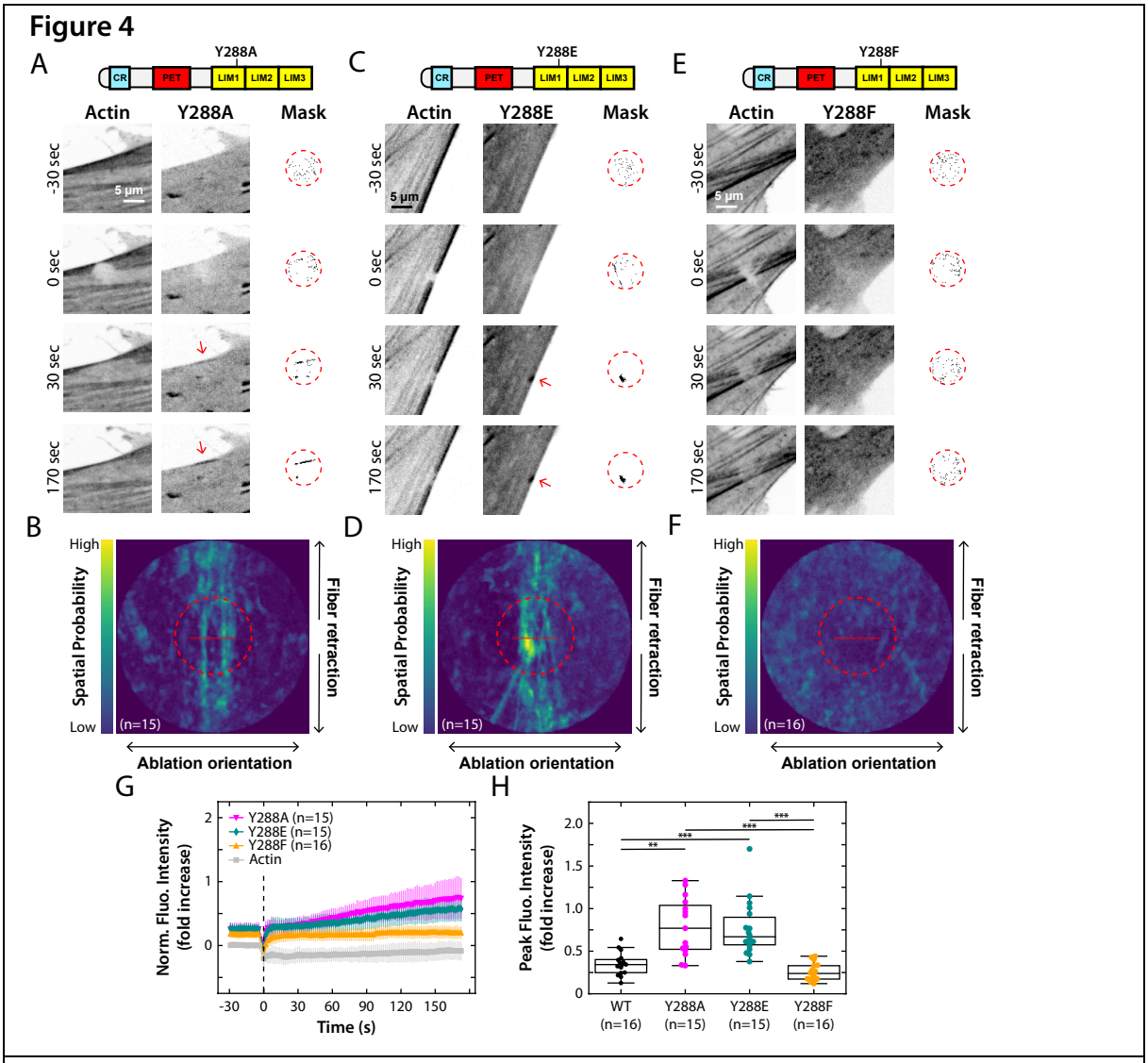

Figure 4: The Y288A and Y288E mutants of testin recognize SFSSs
A, C, E) HFFs co-expressing mApple-actin and either GFP-Y288A (A) GFP-Y288E (C) or GFP-Y288F (E). Magnified inset images (red boxed regions) display the localization of each construct during the timelapse demonstrating relocation to SFSSs of both the Y288A and Y288E mutants (A and C, red arrows), but not the Y288F mutant (E), (Movie S8). Masks show the pixels in the region surrounding the ablation (red dashed circle) that increased the most in intensity compared to their pre-ablation state. **B, D, F)** Spatial probability of recruitment of the Y288 testin mutants in the region of strain. The brightest Y288A and Y288E signals are located in the central region of strain (A and C, dashed circle) whereas the brightest Y288F signal is distributed randomly. Red lines represent the 5 µm laser line used to photo-induce SFSSs. **G)** Average fluorescence intensity traces and standard deviation of the Y288 testin mutants and actin signals in the region of strain indicating recruitment of the Y288A and Y288E mutants, but not the Y288F mutant, to SFSSs. Dashed vertical line indicates the ablation timepoint. **H)** Distribution of the peak fluorescence intensities after SFSS induction for WT testin and the Y288 mutants. **: $p \leq 0.01$, ***: $p \leq 0.001$.

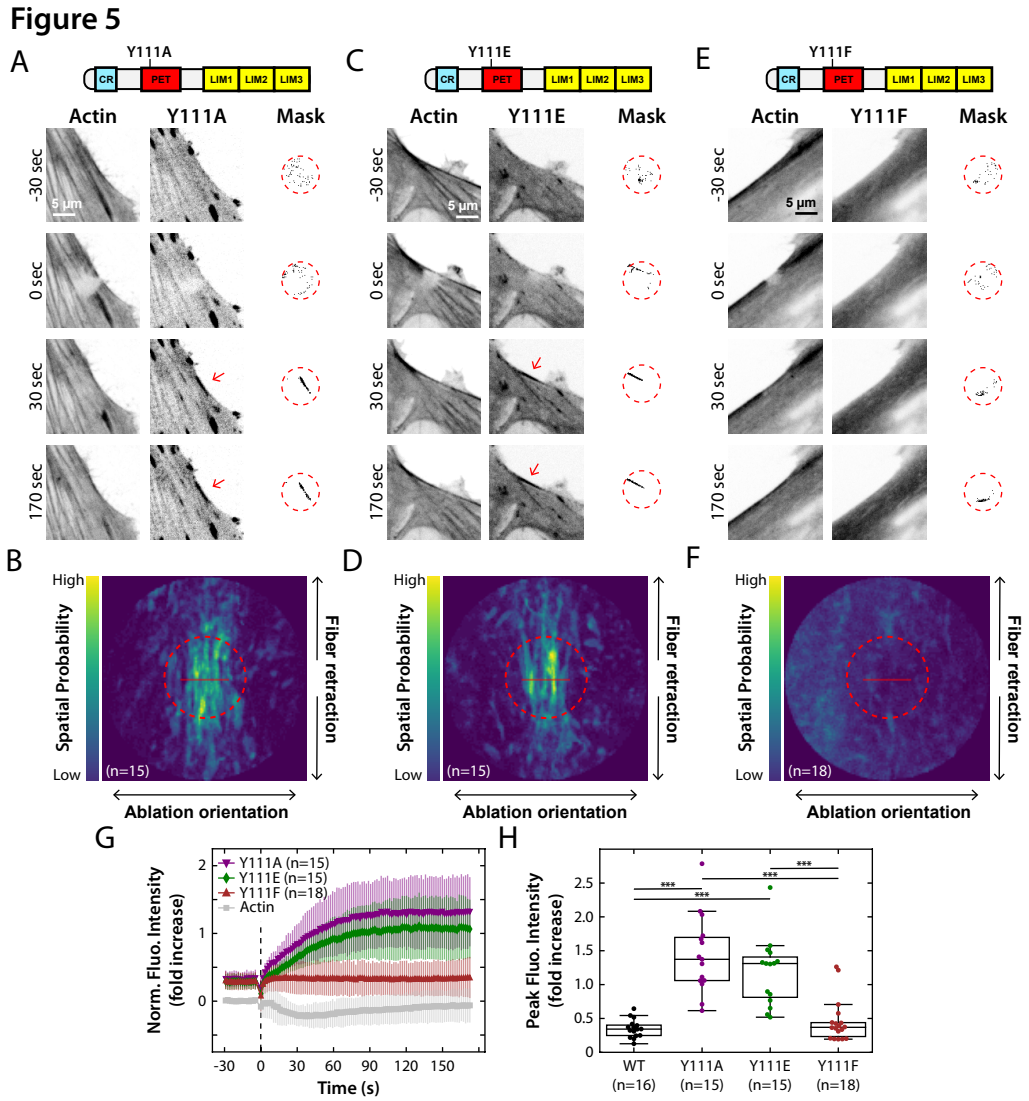

Figure 5: The Y111A and Y111E mutants of testin recognize SFSSs
A, C, E) HFFs co-expressing mApple-actin and either GFP-Y111A (A) GFP-Y111E (C) or GFP-Y111F (E). Magnified inset images (red boxed regions) display the localization of each construct during the timelapse demonstrating relocation to SFSSs of both the Y111A and Y111E mutants (A and C, red arrows), but not the Y111F mutant (E), (Movie S8). Masks show the pixels in the region surrounding the ablation (red dashed circle) that increased the most in intensity compared to their pre-ablation state. **B, D, F)** Spatial probability of recruitment of the Y111 testin mutants in the region of strain. The brightest Y111A and Y111E signals are located in the central region of strain (A and C, dashed circle) whereas the brightest Y111F signal is distributed randomly. Red lines represent the 5 µm laser line used to photo-induce SFSSs. **G)** Average fluorescence intensity traces and standard deviation of the Y111 testin mutants and actin signals in the region of strain indicating recruitment of the Y111A and Y111E mutants, but not the Y111F mutant, to SFSSs. Dashed vertical line indicates the ablation timepoint. **H)** Distribution of the peak fluorescence intensities after SFSS induction for WT testin and the Y111 mutants. ***: $p \leq 0.001$.

Mechanosensitive testin mutants display enhanced FA localization

The observation that specific mutations in the dimerization regions of testin drive it to SFSSs implies these mutations induce a conformation in which the accessibility of the LIM domains is enhanced. Since the truncated LIM domains of testin, but not FL testin, strongly localize to FAs (Fig. 1A,E), we

hypothesized that the mechanosensitive Y111A/E and Y288A/E mutants would display increased FA localization. To investigate this, we co-expressed each of the Y111 and Y288 mutants with paxillin, another FA protein, and assessed their FA localization (Fig. 6A). To quantify FA localization, we calculated the ratio of the fluorescence intensity in FAs and the cytoplasmic region surrounding the FAs for every FA in a given cell (Figs. 6B,S4). In agreement with the results obtained from the laser photoablation assay, we found that FA localization of the mechanosensitive Y111A/E and Y288A/E mutants was significantly increased compared to the non-mechanosensitive Y111F and Y288F mutants, respectively (Fig. 6C). Both F mutants displayed a FA localization that was comparable to or lower than the WT protein (Fig. 6C), which is consistent with their inability to recognize sites of strain.

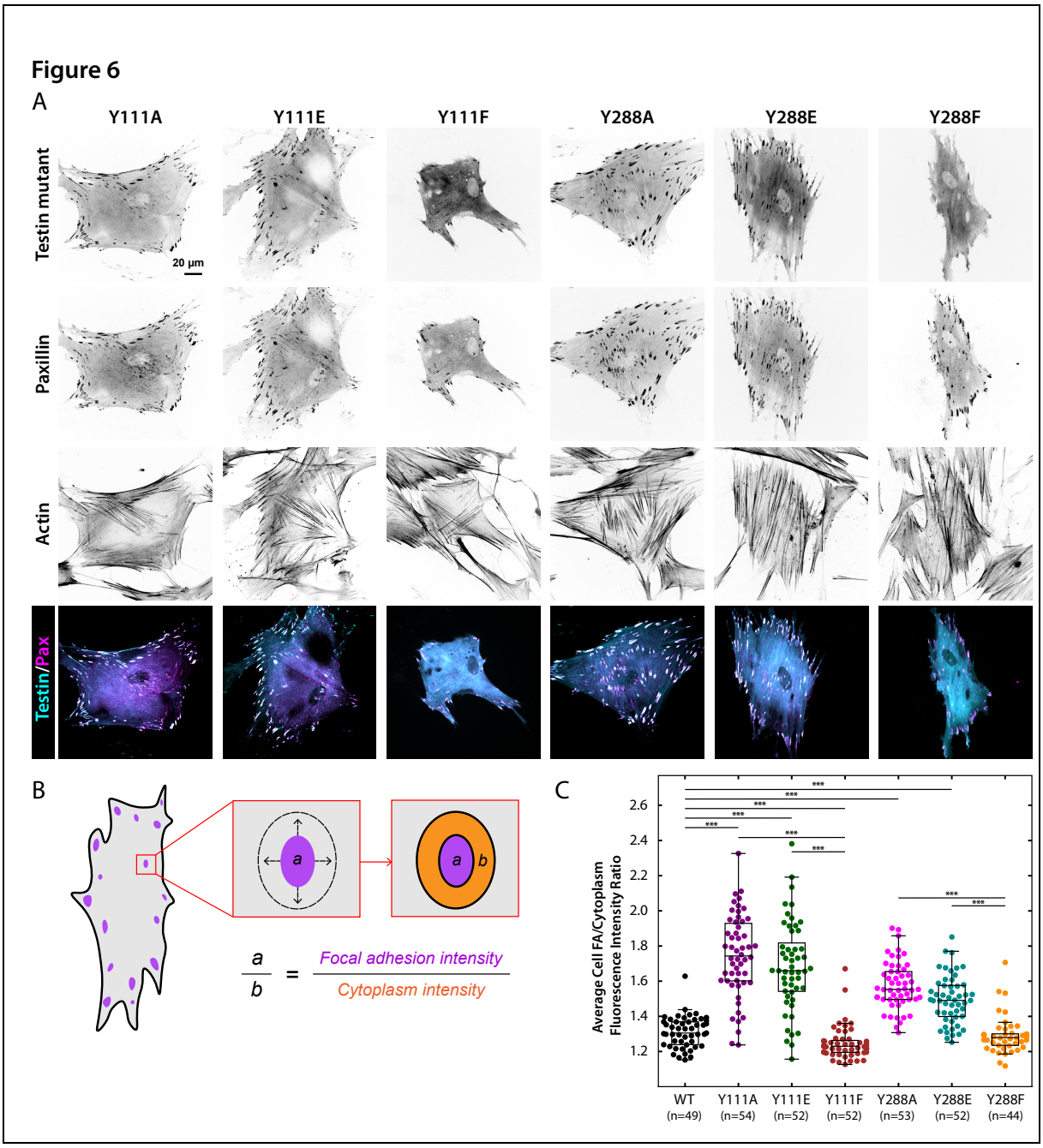

Figure 6: Mechanosensitive testin mutants display increased FA localization
A) Subcellular localization in HFFs of the testin mutants investigated in Fig. 4 and Fig. 5. The mechanosensitive Y111A, Y111E, Y288A and Y288E mutants strongly localize to FAs whereas the non-mechanosensitive Y111F and Y288F mutants display a diffuse cytoplasmic localization and only weak FA localization. GFP-testin, mApple-paxillin and SiR-Actin channels are shown. **B)** Cartoon illustrating the FA localization analysis (Fig. S4). For a given testin variant, the ratio of its fluorescence intensity in the FA region (purple area) and surrounding cytoplasmic region (orange donut) is calculated. **C)** Distribution of the average cellular FA/cytoplasmic fluorescence intensity ratio per testin variant. ***: $p \leq 0.001$.

Cancer-associated point mutations in the PET and LIM2 domains promote testin's mechanosensitivity

Testin has previously been linked to cancer and described as a tumor suppressor based upon observations that its expression is often downregulated in cancer cells (Zhu et al., 2012; Gu et al., 2014; Tatarelli et al., 2000; Tobias et al., 2001). In addition, a limited number of reports also show the existence of cancer-associated mutations in the TES gene (Ma et al., 2010; Weeks et al., 2016; Tatarelli et al., 2000). To further explore this, we used the NIH GDC Data Portal (portal.gdc.cancer.gov) which lists a total of 117 cancer-associated somatic TES mutations identified across 23 different projects, with 58 mutations occurring at the protein level. A significant number of these mutations are located in the dimerization regions, potentially affecting the conformation of the protein. We hypothesized, therefore, that these cancer-associated mutations could also affect the mechanosensitivity of testin.

We chose to investigate two missense mutations located in the PET (E185K, Fig. 7A) and LIM 2 (E306K, Fig. 7B) domains, respectively, and tested whether these mutations altered the mechanosensitivity of testin (Fig. 7C,D; Movie S9). When overexpressed, E185K localized to the cytoplasm and weakly associated with FAs (Fig. 7A). Following strain induction, we observed a moderate but significant recruitment of E185K to SFSSs (Figs. 7C,E,F). Conversely, E306K localized to both FAs and SFs (Fig. 7B) and strongly relocated to SFSSs after strain induction (Fig. 7D-F). Consistent with the Y111A/E and Y288A/E mutants, FA localization of the E306K mutant is significantly higher than E185K and WT testin (Fig.7G).

In contrast to the mechanosensitive Y111A/E and Y288A/E mutants, which only associate with sites of SF strain (Figs. 4,5), the E306K mutant additionally recognizes unstrained SFs displaying a striated localization pattern that colocalized with the SF cross-linking protein alpha-actinin (Fig. 7H). Given the increased SF and FA localization of E306K, we further explored the possibility that this constitutively mechano-active mutant would impact the overall contractility of the cell. Using traction force microscopy, we measured the strain energy per area, a measure of total cell contractility (Oakes et al., 2014), and found no difference between cells expressing either E306K or WT testin. However,

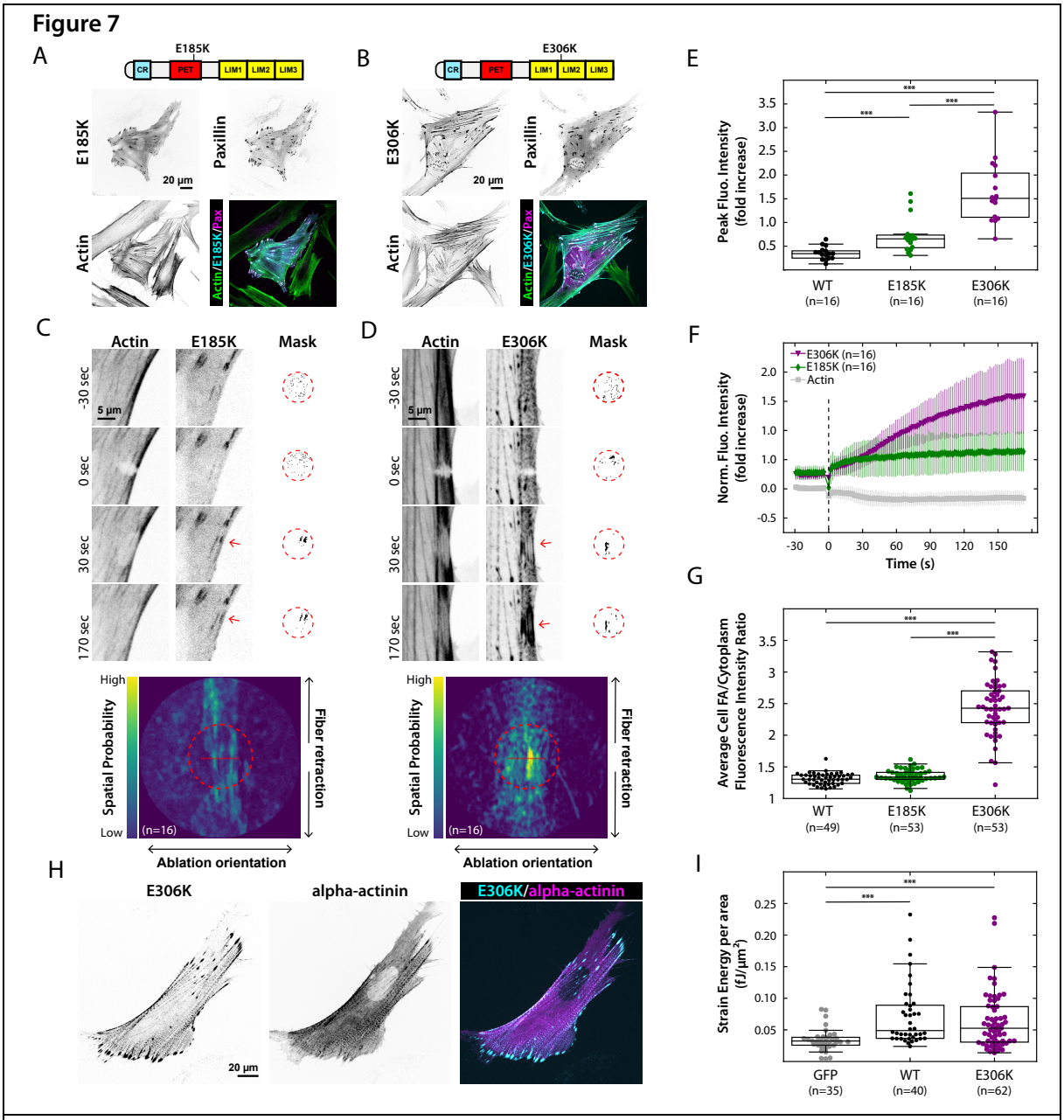

Figure 7: The cancer-associated E185K and E306K mutant of testin relocate to SFSSs
A,B) Subcellular localization of the cancer-associated E185K and E306K mutants in HFFs. The GFP-E185K mutant (A) displays a diffuse cytoplasmic localization and weak FA localization whereas the GFP-E306K mutant (B) is associated with SFs and strongly localizes to FAs. GFP-Testin, mApple-paxillin and SiR-Actin channels are shown. **C,D)** HFFs co-expressing mApple-actin and either GFP-E185K (C) or GFP-E306K (D). Magnified inset images (red boxed regions) display the localization of each construct during the timelapse showing a moderate relocation of GFP-E185K (C, red arrows) but strong relocation of GFP-E306K to SFSSs (D, red arrows), (Movie S9). Masks show the pixels in the region surrounding the ablation (red dashed circle) that increased the most in intensity compared to their pre-ablation state. Spatial probability maps show weak recruitment of E185K but strong recruitment of E306K to the central region of strain (dashed circle). Red lines represent the 5 µm laser line used to photo-induce SFSSs. **E)** Distribution of the peak fluorescence intensities after SFSS induction per testin variant. **F)** Average fluorescence intensity traces and standard deviation of E185K, E306K and actin signal in the region of strain indicating recruitment to SFSSs of both cancer mutants. **G)** Distribution of the average cellular FA/cytoplasmic fluorescence intensity ratio per testin variant demonstrating strong FA localization of the E306K mutant. **H)** Representative images showing colocalization of GFP-E306K and mApple-alpha-actinin at SFs in HFFs. **I)** Traction force microscopy analysis of GFP-WT or GFP-E306K expressing HFFs on fibronectin-coated gels. Distribution of the cellular strain energy per area is shown for both testin variants and GFP control indicating both testin variants increase cellular contractility. ***: $p \leq 0.001$.

compared to the GFP control cells, both E306K and WT testin expressing cells were significantly more contractile (Fig. 7I) illustrating the effect is independent of testin's mechanosensitivity.

Activated RhoA promotes SF localization of testin

The behavior of the various truncations, tyrosine mutants, and cancer mutants in comparison to WT FL testin implies that its mechanosensitivity must be regulated. Since local strain induction at SFs is not sufficient for testin to recognize these sites, we hypothesized that perturbing signaling regulating the actin cytoskeleton at the cellular scale might promote testin's mechanosensitivity. To examine this, we transfected cells with mApple-conjugated FL testin in conjunction with either a constitutively active RhoA (CA-RhoA) or dominant negative RhoA variant (DN-RhoA) to modulate the overall cellular contractility and actin cytoskeleton organization (Fig. 8A (Ridley and Hall, 1992)). Cells expressing the CA-RhoA variant were more contractile (Fig. 8B) and 90% of these cells exhibited SF localization of testin (Fig. 8A,C), compared to 26% of the control cells where testin was primarily cytoplasmic (Fig. 8A,C). Correspondingly, in only 17% of the DN-RhoA expressing cells, testin localized to SFs and was mainly distributed in the cytoplasm.

To explore the role of RhoA in regulating testin's subcellular localization further, we exposed cells to cyclical stretch which has been shown to stimulate RhoA signaling (Lessey et al., 2012). Specifically, cells expressing both actin and testin were plated on fibronectin-coated PDMS membranes and subjected to uniaxial cyclical stretch (2 hours, 15%, 1Hz). Consistent with previous reports (Yoshigi et al., 2005; Livne et al., 2014), we observed reorientation of the cells two hours post stretching, characterized by a typical realignment of the SFs perpendicular to the stretch axis (Fig. 8D). In the majority of the cells exposed to cyclical stretch, testin relocated from the cytoplasm to SFs where it colocalized with actin (Fig. 8D).

To test whether the relocated FL protein can recognize induced sites of strain while already decorating the SFs, we repeated our laser photoablation experiment with FL testin in cells expressing CA-RhoA (Fig. 8E,F, Movie S10). In contrast to the control cells (Fig. 1F-G), we saw recruitment of FL testin to the site of strain (Fig. 8E) and an increase in fluorescence intensity of testin over time (Fig. 8F). Combined, these results indicate that elevated RhoA activity makes FL testin mechanosensitive.

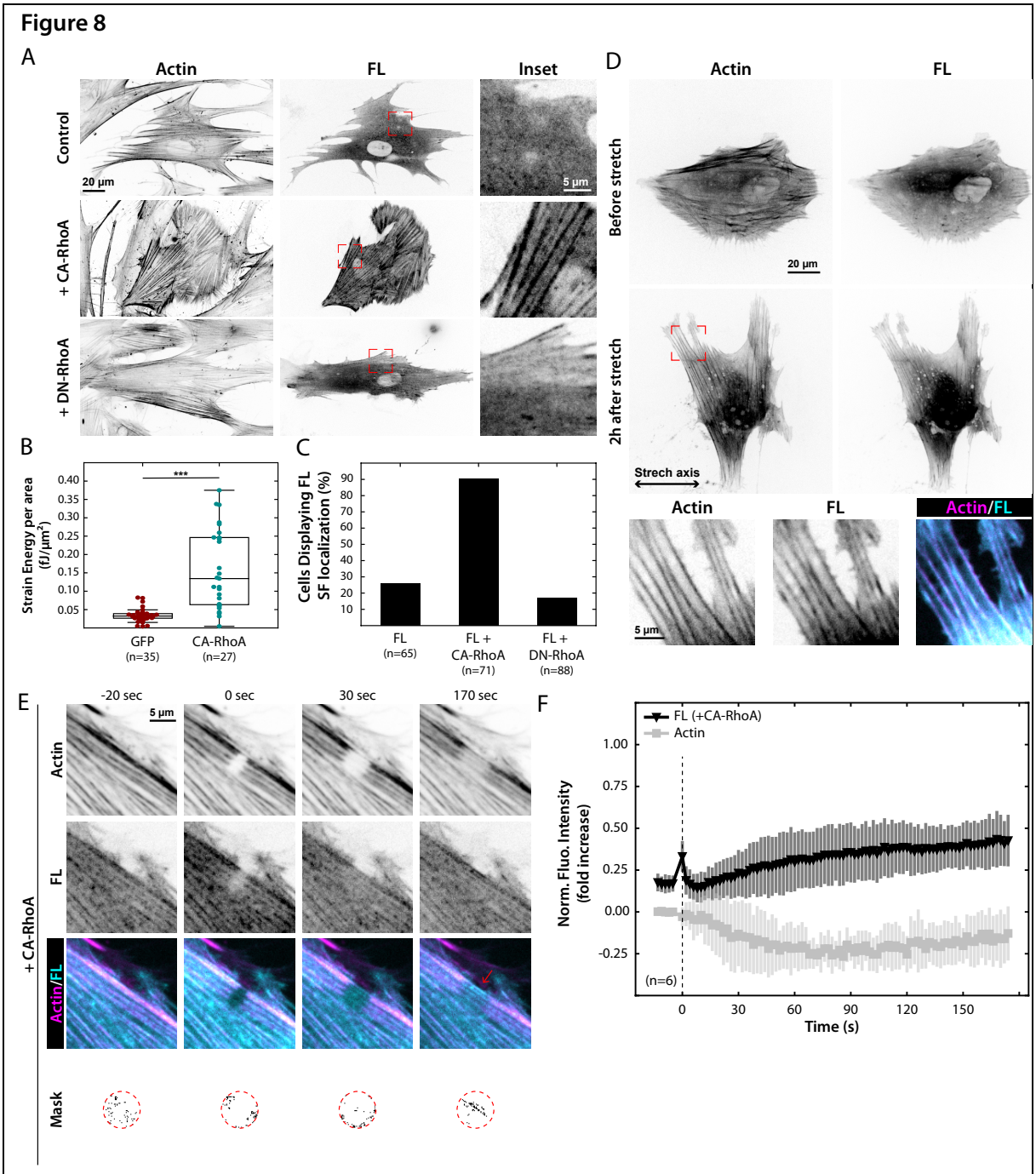

Figure 8: RhoA promotes SF localization of testin

A) HFFs expressing mApple-FL testin and either CA GFP-RhoA or DN GFP-RhoA. In the presence of CA GFP-RhoA, mApple-FL testin relocates to SFs (magnified insets). **B)** Measurement of strain energy per area is shown for both the control (GFP) and CA-RhoA expressing cells. In the presence of CA-RhoA, the overall contractility of the cell is increased. ***: $p \leq 0.001$.**C)** Percentage of HFFs displaying SF localization of mApple-FL testin in the absence or presence of either CA-RhoA or DN-RhoA. **D)** HFFs expressing mApple-FL testin and GFP-actin on PDMS membranes before and after application of uniaxial cyclical stretch (2 hours, 15%, 1Hz). After cyclical stretch, mApple-FL testin relocated to SFs. **E)** HFFs co-expressing mApple-FL testin and CA GFP-RhoA during an ablation. SFs were stained with SiR-Actin. Following strain induction, FL testin relocated to SFSSs (red arrow, Movie S10). **F)** Average fluorescence intensity traces and standard deviation of FL testin and actin in the region of strain indicating recruitment of FL testin to SFSSs.

Discussion

Our data reveal that the mechanosensitivity of the LDP testin is highly regulated, likely through modification of its conformational state, allowing cells to potentially control its spatiotemporal behavior through signaling molecules such as RhoA. Over the last decade, it has become more apparent that the mechanical state of filamentous actin (tension, curvature, torsion) affects the binding and activity of many actin-binding proteins (Jégou and Romet-Lemonne, 2021; Zimmermann et al., 2017). Recent work (Sun et al., 2020; Winkelman et al., 2020) has highlighted that a conserved mechanism in LIM domains confers mechanosensitivity to proteins from the FHL, zyxin and paxillin families among others to sense strained actin filaments. The LDP testin appears unique in that the FL protein resides primarily in the cytoplasm, while its N-terminal half recognizes unstrained actin filaments and its C-terminal half recognizes strained actin filaments (Figs. 1-2). Although the functional consequences of this unique feature are currently unknown, we speculate that testin acts as a bifunctional scaffold protein in mechanically stressed actin-rich structures.

In contrast to zyxin and other LDPs, which require 3 successive LIM domains to recognize SFSSs (Sun et al., 2020; Winkelman et al., 2020), we show that each of the individual LIM domains of testin can recognize SFSSs on their own (Figs. 1J, S2). This discrepancy between testin and other LDPs may be due to unique sequence motifs present in testin's LIM domains, which only share ~25% sequence identity with the LIM domains of zyxin based on their UniProt database sequences. We cannot rule out that testin's individual LIM domains are indirectly associating with strained actin via recruitment by other SFSS proteins. The LIM domains of testin have been shown to interact with zyxin, VASP and alpha-actinin (Garvalov et al., 2003; Sala et al., 2017b), which are all found in SFSSs (Smith et al., 2011). This scenario, however, seems unlikely since we find that LIM 1-2-3 recruitment to SFSSs is independent of zyxin (Fig. 3F-H) and that the recruitment kinetics of the individual LIM domains of testin are all comparable to the recruitment kinetics of LIM 1-2-3 (Fig. S3). Together these findings suggest that the individual LIM domains of testin recognize the same molecular mark of strained actin as the multi-LIM domain variant and that the increased magnitude of recruitment of LIM 1-2-3 results from the additive contribution of each LIM domain.

While the N-terminal half of testin clearly recognizes unstrained actin filaments, it is not mechanosensitive on its own (Fig. 2). We hypothesize that it might play a role in maintaining SF homeostasis in conjunction with the LIM domains. Certain actin-binding proteins have indeed been shown to form co-complexes with either the LIM domains (e.g. Ena/VASP proteins, (Garvalov et al., 2003; Boëda et al., 2007; Sala et al., 2017b)) or N-terminal domains (e.g. calponin-2, (Sala et al., 2017b)) of testin, showing that both halves could contribute to the recruitment of these proteins. Future studies will be required to investigate the potential function of testin in maintaining the mechanical integrity of SFs.

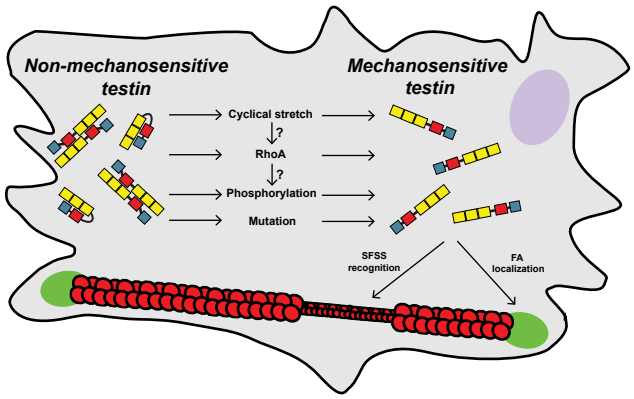

Figure 9: Model of the mechanosensitivity mechanisms of testin
Non-mechanosensitive testin is mainly cytoplasmic, likely adopting a dimeric or closed conformation. Regulatory mechanisms (cyclical stretch, elevated RhoA activity, phosphorylation or disease-associated mutations), alter testin's conformation conferring mechanosensitivity to the protein and allowing it to relocate to SFSSs and FAs.

The numerous point mutations which confer mechanosensitivity to testin suggest that this function of the protein can be regulated. High throughput mass-spec analyses provide evidence that both Y288 and Y111 can be phosphorylated (www.phosphosite.org), and phosphomimetic mutations of these tyrosines to glutamic acid make testin mechanosensitive. That the alanine mutants are also mechanosensitive, while the phenalylalanine mutants are not, however, suggests a structural change is more likely driving this behavior than phosphorylation. Previous work has shown that, in addition to its monomeric open and closed conformations (Garvalov et al., 2003), testin dimerizes through a direct interaction between an N-terminal region containing the PET domain, where Y111 is located, and the C-terminal first two LIM domains, which contain Y288 (Sala et al., 2017a). In particular, it was shown that a Y288A mutation hampers dimerization of testin (Sala et al., 2017a). It is therefore likely that the loss of the aromatic ring in the E and A mutants causes a conformational change in the protein which impacts dimerization and frees the mechanosensitive LIM domains to recognize SFSSs. The differences in kinetics we see between mutations at positions Y288 and Y111 are likely related to their local effect on the conformation of the protein and its associated impact on dimerization. Structural studies, however, will be necessary to confirm and elucidate the underlying mechanisms.

That conformational changes regulate testin's mechanosensitivity is further supported by the behavior of the cancer-associated E185K and E306K mutants, which are also located in the PET and LIM domains, respectively. These point mutations had drastic effects on the localization of testin, driving it to SFSSs, and in the case of E306K, to unstrained SFs in a stippled pattern reminiscent of alpha-actinin or zyxin. While the functional implications of these mutations and their potential contributions to cancer are currently unknown, it is remarkable that all the mechanosensitive variants of testin

showed increased localization to FAs. This is consistent with our previous observation that the regions where SFs are coupled to FAs likely contain sites of strained actin filaments (Oakes et al., 2017), though it does not preclude that testin could be binding other FA proteins. A similar tension-dependent recruitment of testin to focal adherens junctions has been observed in endothelial cells, raising the possibility that testin plays an analogous role in cell-cell junctions (Oldenburg et al., 2015).

While the mechanosensitive E306K mutant recognizes increased strain in the actin cytoskeleton, it does not further increase the overall force generation capabilities of the cell compared to the effect of WT testin. Somewhat surprisingly, both E306K and WT testin increased the overall contractility of the cell, compared to the GFP control cells (Figs. 7I). This demonstrates that the ability of testin to sense strain is decoupled from its contribution to cellular force generation. Overexpression of a constitutively active RhoA variant, however, did cause WT testin to relocate to SFs and recognize SFSSs (Fig. 8). This suggests that signaling proteins downstream of RhoA potentially affect testin's conformational state thereby changing its mechanosensitive behavior as well (Fig. 9). The underlying mechanisms of how RhoA activation modulates testin's mechanosensitivity still need to be explored, but previous reports have established that many downstream effectors of RhoA, including kinases, show increased activity in response to mechanical forces (Lessey et al., 2012; Torsoni et al., 2005).

Our results imply that testin is only associated with strained SFs under certain conditions and thus we propose that its mechanosensitivity is actively regulated by the cell. Furthermore, our findings raise the possibility that similar regulatory mechanisms apply to other LDPs, of which only a subset have been identified as mechanosensitive. For example, a recent study has shown that LIMD1, in contrast to its LIM domains, is incapable of recognizing tensed SFs (Sun et al., 2020), suggesting that its mechanosensitivity is likely also context dependent. These insights may also help clarify the functional role of testin in cells. While it has been proposed to act as a tumor suppressor, the molecular mechanisms underlying testin's role in cancer remain poorly understood. Testin is known to affect actin-driven mechanical processes, including cell spreading, cell migration and proliferation (Griffith et al., 2004; Li et al., 2016; Sala et al., 2017b). Connecting testin's mechanosensitivity to RhoA activity provides important context for interpreting testin's role in these and other cellular processes. Future research will be required to assess how regulation or dysregulation of testin's mechanosensitivity affects these many cellular functions and diseases that it is implicated in. It remains clear, however, that regulation of LDPs represent an intriguing and broad mechanism for cells to control mechanotransduction activity.

Abbreviations

CA: constitutively active; CR: cysteine rich; DN: dominant-negative; FA: focal adhesion; FHL: four-and-a-half LIM; FL: full-length; HFF: human foreskin fibroblast; LDP: LIM domain protein; LIM: Lin-11, Isl-1, Mec-3; MEF: mouse embryonic fibroblast; Polydimethylsiloxane: PDMS; PET: Prickle, Espinas, Testin; SF: stress fiber; SFSS: stress fiber strain site

Acknowledgements

We thank the Beach lab at the Loyola University Chicago, Maywood, IL for the many helpful discussions. We thank the Ampe lab at the University of Gent for their critical input and certain testin constructs. We thank Dr. Evelyne Friederich and Dr. Elisabeth Schaffner-Reckinger from the University of Luxembourg for certain testin constructs. We are also thankful to the Beckerle lab at the University of Utah, Salt Lake City, UT for providing us with the zyxin antibody, mcherry-zyxin construct and both WT and zyxin$^{(-/-)}$ MEFs. This work was supported in part by a National Science Foundation CAREER Award (#2000554) to P.W.O. The authors declare no competing financial interests.

Author Contributions

Conceptualization, data curation, formal analysis, investigation, methodology, software, validation, visualization and writing: Stefano Sala and Patrick Oakes.

Materials and methods

Mammalian expression vectors and cloning

For expression as GFP-fusion proteins, cDNAs encoding full-length (FL) testin (amino acids 1-421), full-length Y288A (Y288A substitution), NT (CR and PET domains, amino acids 1-233), LIM 1-2-3 (amino acids 231-421) , LIM 1 (amino acids 234-299), LIM 2 (amino acids 299-354) and LIM 3 (amino acids 361-421) were cloned into the multiple cloning site of pEGFP-N3 or pEGFP-C3 (Clontech) as previously described (Sala et al., 2017a; b). For expression as mApple-fusion proteins, cDNA encoding full-length testin (amino acids 1-421) and NT (amino acids 1-233) were amplified from the full-length testin pEGFP-N3 vector (Forward primer: 5'-CCGCTCGAGCTATGGACCTG-3', Reverse primer FL: 5'-CGGGATCCCTAAGACATCCTCTTC-3', Reverse primer NT: 5'-CGGGATCCCTATTGAGTTCTTTTGTGCTC-3') and cloned into the mApple-C1 vector (Addgene plasmid # 54631) using the XhoI and BamHI restriction sites. Y111E, E185K and E306K substitutions were introduced into the full-length testin pEGFP-N3 vector (Forward primer Y111E: 5'-TACAGTTACCGAAGAGTGGGCTC-3', Reverse primer Y111E: 5'-TTGATGGAGACATTCTTC-3', Forward primer E185K: 5'-ATATAAGAGCAAAGCTCTGGG-3', Reverse primer E185K: 5'-TTCTTCACAAACTGCTCC-3', Forward primer E306K: 5'-TGGCTGTGACAAGCTGATATTCAG-3', Reverse primer E306K: 5'-GCACATCGGGGTTTCTCG-3') using the Q5 site-directed mutagenesis kit (E0554S, New England Biolabs) to generate point mutants. Y111A, Y111F, Y288E and Y288F point mutants of GFP-fused full-length testin were a kind gift of Dr. Evelyne Friederich and Dr. Elisabeth Schaffner-Reckinger (University of Luxembourg, Luxembourg). mCherry-zyxin was a kind gift of Dr. Mary Beckerle's lab (University of Utah, Salt Lake City, UT). pcDNA3-EGFP-RhoA-T19N (Addgene plasmid # 12967) and pcDNA3-EGFP-RhoA-Q63L (Addgene plasmid # 12968) were kind gifts from Gary Bokoch. mApple-C1 (Addgene plasmid # 54631), mApple-actin (Addgene plasmid # 54862), mApple-alpha-actinin (Addgene plasmid # 54865), mApple-paxillin (Addgene plasmid # 54935) and GFP-actin (Addgene plasmid # 56421) vectors were a kind gift from Michael Davidson. All constructs were verified by sequencing.

Cell culture and transfection

Human foreskin fibroblasts (HFF) were obtained from ATCC (CRL-2522™). Mouse embryonic fibroblasts (MEF) and zyxin$^{(-/-)}$ MEFs were a kind gift of Mary Beckerle's lab (University of Utah, Salt Lake City, UT). HFFs and MEFs were cultured in Dulbecco's Modified Eagle Medium (MT10013CV, Corning) supplemented with 10% fetal bovine serum (MT35-010-CV, Corning) and 1% antibiotic-antimycotic solution (MT30004CI, Corning) at 37°C and 5% CO_2. 24 hours prior to each experiment, HFFs were transfected with 5 µg total DNA using a Neon electroporation system (ThermoFisher Scientific) and plated on polyacrylamide gels (traction force microscopy),

polydimethylsiloxane (PDMS) membranes (stretching experiments) or glass coverslips (laser photoablation, quantification of focal adhesion localization). 48 hours prior to laser photoablation, zyxin$^{(-/-)}$ MEFs were transfected with 5 µg total DNA using the Fugene® 6 transfection reagent (E2691, Promega) and plated on glass coverslips.

Live cell imaging

Cells were imaged in culture media supplemented with 20 mM HEPES (SH3023701, HyClone) at 37°C, with or without 1µM SiR-Actin (CY-SC001, Cytoskeleton), on a Marianas Imaging System (Intelligent Imaging Innovations) consisting of an Axio Observer 7 inverted microscope (Zeiss) attached to a W1 Confocal Spinning Disk (Yokogawa) with Mesa field flattening (Intelligent Imaging Innovations), Phasor photomanipulation unit (Intelligent Imaging Innovations), motorized X,Y stage (ASI) and Prime 95B sCMOS (Photometrics) camera. Illumination was provided by a TTL triggered multifiber laser launch (Intelligent Imaging Innovations) consisting of 405, 488, 561, and 637 lasers, using 63X 1.4 NA Plan-Apochromat objective (Zeiss). Temperature and humidity were maintained using a Bold Line full enclosure incubator (Oko Labs). The microscope was controlled using Slidebook 6 Software (Intelligent Imaging Innovations).

Laser photoablation and quantitative analysis of stress fiber strain site recruitment

Prior to initiating a timelapse, a 5µm linear region was drawn in Slidebook over the SFs that were to be damaged. Cells were imaged for 3 minutes and 30 seconds alternating between the actin and testin channels with images taken approximately every 2 seconds. After 30 seconds of imaging the steady state, the marked 5µm region was illuminated with the 405 laser at a power of 370 µW for 1.5 seconds to induce a SFSS via photoablation. The remainder of the timelapse was then imaged.

Images were analyzed in python following a scheme laid out graphically in Fig. S1A. Each timelapse was first broken into two stacks representing the testin channel and the actin channel. Each stack was first flat field corrected and photobleach corrected (Payne-Tobin Jost and Waters, 2019). The testin channel was then registered using the whole image via an efficient sub-pixel registration algorithm (Guizar-sicairos et al., 2008). The calculated registration shifts from the testin channel were then applied to the actin channel, and both channels were cropped to a region of 121 x 121 pixels (~21 µm x 21 µm) centered on the ablation region. For each channel an average intensity image was created by averaging the frames in the stack prior to the ablation event. A relative difference was determined at each time point by subtracting the reference image from a given frame, and then dividing by the reference image. A mask of the 5% brightest points relative to the reference image in the testin channel was created for each time point. The average value of the masked points in each channel was then plotted as a function of time to create a trace of the normalized fluorescence intensity for each movie.

Average traces were created by averaging the traces from multiple movies and plotting the mean +/- the std deviation for each time point. To calculate the $t_{1/2}$ value the average trace curve starting from $t = 0$ was fitted to the following equation: $I(t) = A - Be^{(-t/k)}$, where $t_{1/2} = \ln\frac{A}{2B} * -k$. Fits are shown in Fig. S3 and calculated fit parameters for each testin construct can be found in Table S1.

The offset seen in the testin channel signal trace (e.g. Fig. 1C) is a product of making a mask of the 5% pixels that are brightest compared to the reference image. Because the location of the strain site is dependent on the local architecture of the actin cytoskeleton, we couldn't simply choose a predetermined region of interest to measure recruitment. By using the pixels that increased in intensity the most relative to the reference image, we were able to create dynamic masks that could identify recruitment independent of the location within the ablation region. Figs. S1B,C show how that offset changes as the number of pixels used in the mask is increased. The trace in the actin channel does not show such an offset because the masked pixels were chosen based on the testin image. For the traces in the control experiments using zyxin (Fig. 1D,H), the masked points were chosen using the zyxin channel and then applied to the testin and actin channels.

To create the spatial probability maps, we took the masks for a given movie and summed them across the entire stack (Fig. S1D). The resulting image was then rotated to align the direction of the ablation horizontally and then averaged across all the movies for a given condition. The following number of ablations were performed for each condition: FL – 16; LIM 1-2-3 – 14; LIM 1 – 15; LIM 2 – 16; LIM 3 – 14; NT – 15; Y111A – 15; Y1111E – 15; Y111F – 18; Y288A – 15; Y288E – 15; Y288F – 16; E185K – 16; E306K – 16; FL + CA RhoA – 6; Zyxin + LIM 1-2-3 – 6; Zyxin + FL – 5; Zyxin (-/-) + LIM 1-2-3 – 6.

Traction force microscopy and analysis

Traction force microscopy was performed as described previously (Sabass et al., 2008; Oakes et al., 2017). Coverslips were prepared by incubating with a 2% solution of 3-aminopropyltrimethyoxysilane (313255000, Acros Organics) diluted in isopropanol, followed by fixation in 1% glutaraldehyde (16360, Electron Microscopy Sciences) in ddH_20. Polyacrylamide gels (shear modulus: 16 kPa – final concentrations of 12% Acrylamide (1610140, Bio-Rad) and 0.15% Bis-acrylamide (1610142, Bio-Rad)) were embedded with 0.04 µm fluorescent microspheres (F8789, Invitrogen) and polymerized on activated glass coverslips for 1 hour at room temperature. After polymerization, gels were rehydrated for 45 minutes and coupled to human plasma fibronectin (FC010, Millipore) for 1 hour at room temperature using the photoactivatable cross-linker Sulfo-Sanpah (22589, Pierce Scientific). Following fibronectin cross-linking, cells were plated on the gels and allowed to spread overnight. The next day, images were taken of both the cells and underlying fluorescent beads. Number of cells imaged per condition: Fig. 7I - (GFP: 35, FL-GFP: 40, E306K-GFP: 62); Fig 8B - (GFP: 35, CA GFP-

RhoA: 27). Following imaging, cells were removed from the gel using 0.05% SDS and a reference image of the fluorescent beads in the unstrained gel was taken.

Analysis of traction forces was performed using code written in Python according to previously described approaches (Sabass et al., 2008; Hanke et al., 2018). Prior to processing, images were flat field corrected and the reference bead image was aligned to the bead image with the cell attached. Displacements in the beads were calculated using an optical flow algorithm in OpenCV (Open Source Computer Vision Library, https://github/itseez/opencv) with a window size of 8 pixels. Traction stresses were calculated using the FTTC approach (Butler et al., 2002; Sabass et al., 2008) as previously described with a regularization parameter of 6.1 x 10^-4. The strain energy was calculated by summing one half the product of the strain and traction vectors in the region under the cell (Oakes et al., 2014) and normalized by the cell area as measured using the GFP image of the cell.

Quantification of FA localization

Analysis was performed using custom code written in Python and outlined graphically in Fig. S4. Briefly, thresholding of the GFP-testin intensity images was performed to create a cell mask. mApple-paxillin intensity images were flat field-corrected and a Laplacian of Gaussian filter was applied for edge detection and creation of a FA mask. FAs were dilated using a 10x10 square structuring element and multiplied by the inverted cell mask to create a cytoplasmic donut-shaped region surrounding the FAs. The FA mask and surrounding donut mask were used to calculate the ratio (FA/cytoplasm ratio) of the average intensity in the corresponding regions of the testin intensity image. The average FA/cytoplasm ratio was then calculated per cell. Per GFP-testin variant, a total of *n* cells was analyzed (WT: 49, Y111A: 54, Y111E: 52, Y111F: 52, Y288A: 53, Y288E: 52, Y288F: 44, E306K: 53, E185K: 51).

Western blotting

Cell lysates were analyzed using SDS-PAGE and 10% polyacrylamide gels, and transferred to a Whatman Protran nitrocellulose membrane (1620115, Biorad). Membranes were blocked for 1 hour at room temperature in Odyssey blocking buffer (92740000, LI-COR). After blocking, membranes were incubated at 4 °C overnight with primary antibody in Odyssey blocking buffer. Subsequently, membranes were washed 3 times in PBS containing 0.1% Tween 20 (BP337-100, Fisher Scientific) for 10 min and incubated for 1 hour at room temperature with secondary antibody in Odyssey blocking buffer. Finally, membranes were washed 3 times in PBS/Tween 20 for 10 min and rinsed in Milli-Q-H_2O. The Odyssey® Classic infrared imaging device (LI-COR) was used for signal detection. The following primary antibodies were used: mouse anti-GAPDH (MA5-15738, Thermofisher, 1/3000 dilution) and rabbit anti-zyxin (ABD1463, Millipore, 1/1000 dilution) which was a kind gift of Mary Beckerle's lab (University of Utah, Salt Lake City, UT). The following LI-COR secondary antibodies

were used at a 1/10000 dilution: goat anti-rabbit IRdye800 (925-32211), goat anti-mouse IRdye680 (925-68070).

Cell stretcher

50 mm x 40 mm PDMS membranes (PF-60-X4, Gel-Pak) were plasma-activated for 10 minutes using a plasma cleaner (PDC-32G, Harrick Plasms) prior to being incubated with 0.05 M sulfo-NHS (Thermofisher, PI24510) and 0.1 M EDC (Thermofisher, PI22980) in a 0.05 M MES (Thermofisher, BP300 100) with 0.5 M NaCl solution at pH 6 for 15 minutes at room temperature. Subsequently, membranes were rinsed with Milli-Q-H2O and incubated with 25 µg/ml human plasma fibronectin (FC010, Millipore) for 1 hour at room temperature. Following fibronectin coating, cells were plated on the PDMS membranes and allowed to spread overnight. Uniaxial cyclical stretch (15% stretch, 1 Hz) was applied to the cells for 2 hours at 37°C and 5% CO_2 using a custom-made stretching device, plans of which are available upon request.

Statistical analysis

Statistical analyses were performed in Python using the nonparametric multiple comparison Kruskal−Wallis one-way ANOVA test with Dunn's posthoc method. Details about sample size and p-values are included in the Materials and Methods section and figure legends.

Software

All images were exported from Slidebook as 16-bit TIFF files and analyzed in python. All custom code is available at (https://github.com/OakesLab).

Supplemental Material

Table S1: Subcellular localization and recruitment magnitude/kinetics of the testin variants used in this study

Figure S1: Graphical representation of laser photoablation analysis workflow

Figure S2: The individual LIM domains of testin are sufficient to recognize stress fiber strain sites

Figure S3: Exponential curve fitting of the average fluorescence intensity traces of mechanosensitive testin variants

Figure S4: Graphical representation of focal adhesion localization analysis workflow

Movie S1: The LIM domains of testin, but not the full-length or N-terminal half of the protein, recognize SFSSs.

Movie S2: Testin's LIM domains, but not the full-length protein, colocalize with zyxin at SFSSs.

Movie S3: Each individual LIM domain of testin relocates to SFSSs.

Movie S4: The N-terminal domains and C-terminal LIM domains of testin recognize different mechanical states of SFs.

Movie S5: Photodamaged SFs are not fully severed and remain under tension

Movie S6: The LIM domains of testin recognize strained but not severed SFs

Movie S7: Testin's LIM domains relocate to SFSSs in a zyxin independent manner

Movie S8: The Y111A/E and Y288A/E point mutants of testin relocate to SFSSs

Movie S9: The cancer-associated E185K and E306K mutants of testin recognize SFSSs

Movie S10: RhoA drives testin to SFSSs

References

Blanchoin, L., R. Boujemaa-Paterski, C. Sykes, and J. Plastino. 2014. Actin dynamics, architecture, and mechanics in cell motility. *Physiol. Rev.* 94:235–263. doi:10.1152/physrev.00018.2013.

Boëda, B., D.C. Briggs, T. Higgins, B.K. Garvalov, A.J. Fadden, N.Q. McDonald, and M. Way. 2007. Tes, a Specific Mena Interacting Partner, Breaks the Rules for EVH1 Binding. *Mol. Cell*. 28:1071–1082. doi:10.1016/j.molcel.2007.10.033.

Boëda, B., P.P. Knowles, D.C. Briggs, J. Murray-Rust, E. Soriano, B.K. Garvalov, N.Q. McDonald, and M. Way. 2011. Molecular recognition of the Tes LIM2-3 domains by the actin-related protein Arp7A. *J. Biol. Chem.* 286:11543–11554. doi:10.1074/jbc.M110.171264.

Brown, A.E.X., and D.E. Discher. 2009. Conformational Changes and Signaling in Cell and Matrix Physics. *Curr. Biol.* 19:R781–R789. doi:10.1016/j.cub.2009.06.054.

Butler, J.P., I.M. Toli-Nørrelykke, B. Fabry, and J.J. Fredberg. 2002. Traction fields, moments, and strain energy that cells exert on their surroundings. *Am. J. Physiol. - Cell Physiol.* 282:595–605. doi:10.1152/ajpcell.00270.2001.

Cai, Y., and M.P. Sheetz. 2009. Force propagation across cells: mechanical coherence of dynamic cytoskeletons. *Curr. Opin. Cell Biol.* 21:47–50. doi:10.1016/j.ceb.2009.01.020.

Das, T., K. Safferling, S. Rausch, N. Grabe, H. Boehm, and J.P. Spatz. 2015. A molecular mechanotransduction pathway regulates collective migration of epithelial cells. *Nat. Cell Biol.* 17:276–287. doi:10.1038/ncb3115.

Drusco, A., N. Zanesi, C. Roldo, F. Trapasso, J.L. Farber, L.Y. Fong, and C.M. Croce. 2005. Knockout mice reveal a tumor suppressor function for Testin. *Proc. Natl. Acad. Sci. U. S. A.* 102:10947–10951. doi:10.1073/pnas.0504934102.

Engler, A.J., S. Sen, H.L. Sweeney, and D.E. Discher. 2006. Matrix Elasticity Directs Stem Cell Lineage Specification. *Cell*. 126:677–689. doi:10.1016/j.cell.2006.06.044.

Fabry, B., and J.J. Fredberg. 2007. Mechanotransduction, asthma and airway smooth muscle. *Drug Discov. Today Dis. Model.* 4:131–137. doi:10.1016/j.ddmod.2007.12.003.

Garvalov, B.K., T.E. Higgins, J.D. Sutherland, M. Zettl, N. Scaplehorn, T. Köcher, E. Piddini,

G. Griffiths, and M. Way. 2003. The conformational state of Tes regulates its zyxin-dependent recruitment to focal adhesions. *J. Cell Biol.* 161:33–39. doi:10.1083/jcb.200211015.

Gill, G.N. 1995. The enigma of LIM domains. *Structure*. 3:1285–1289. doi:10.1016/S0969-2126(01)00265-9.

Goldmann, W.H. 2016. Role of vinculin in cellular mechanotransduction. *Cell Biol. Int.* 40:241–256. doi:10.1002/cbin.10563.

Griffith, E., A.S. Coutts, and D.M. Black. 2004. Characterisation of Chicken TES and Its Role in Cell Spreading and Motility. *Cell Motil. Cytoskeleton*. 57:133–142. doi:10.1002/cm.10162.

Gu, Z., G. Ding, K. Liang, H. Zhang, G. Guo, L. Zhang, and J. Cui. 2014. TESTIN suppresses tumor growth and invasion via manipulating cell cycle progression in endometrial carcinoma. *Med. Sci. Monit.* 20:980–987. doi:10.12659/MSM.890544.

Guizar-sicairos, M., S.T. Thurman, and J.R. Fienup. 2008. Efficient subpixel image registration algorithms. *Opt. Lett.* 33:156–158.

Hadzic, E., M. Catillon, A. Halavatyi, S. Medves, M. Van Troys, M. Moes, M.A. Baird, M.W. Davidson, E. Schaffner-Reckinger, C. Ampe, and E. Friederich. 2015. Delineating the tes interaction site in zyxin and studying cellular effects of its disruption. *PLoS One*. 10:1–27. doi:10.1371/journal.pone.0140511.

Haining, A.W.M., T.J. Lieberthal, and A. Del Río Hernández. 2016. Talin: A mechanosensitive molecule in health and disease. *FASEB J.* 30:2073–2085. doi:10.1096/fj.201500080R.

Hanke, J., D. Probst, A. Zemel, U.S. Schwarz, and S. Köster. 2018. Dynamics of force generation by spreading platelets. *Soft Matter*. 14:6571–6581. doi:10.1039/c8sm00895g.

Hemmatian, H., A.D. Bakker, J. Klein-Nulend, and G.H. van Lenthe. 2017. Aging, Osteocytes, and Mechanotransduction. *Curr. Osteoporos. Rep.* 15:401–411. doi:10.1007/s11914-017-0402-z.

Heydemann, A., and E.M. McNally. 2007. Consequences of Disrupting the Dystrophin-Sarcoglycan Complex in Cardiac and Skeletal Myopathy. *Trends Cardiovasc. Med.* 17:55–59. doi:10.1016/j.tcm.2006.12.002.

Hoffman, L.M., C.C. Jensen, A. Chaturvedi, M. Yoshigi, and M.C. Beckerle. 2012. Stretch-induced actin remodeling requires targeting of zyxin to stress fibers and recruitment of actin regulators. *Mol. Biol. Cell*. 23:1846–1859. doi:10.1091/mbc.E11-12-1057.

Hoffman, L.M., C.C. Jensen, S. Kloeker, C.L.A. Wang, M. Yoshigi, and M.C. Beckerle. 2006. Genetic ablation of zyxin causes Mena/VASP mislocalization, increased motility, and deficits in actin remodeling. *J. Cell Biol.* 172:771–782. doi:10.1083/jcb.200512115.

Iskratsch, T., H. Wolfenson, and M.P. Sheetz. 2014. Appreciating force and shape-the rise of mechanotransduction in cell biology. *Nat. Rev. Mol. Cell Biol.* 15:825–833. doi:10.1038/nrm3903.

Jégou, A., and G. Romet-Lemonne. 2021. Mechanically tuning actin filaments to modulate the action of actin-binding proteins. *Curr. Opin. Cell Biol.* 68:72–80. doi:10.1016/j.ceb.2020.09.002.

Kanchanawong, P., G. Shtengel, A.M. Pasapera, E.B. Ramko, M.W. Davidson, H.F. Hess, and C.M. Waterman. 2010. Nanoscale architecture of integrin-based cell adhesions. *Nature*. 468:580–584. doi:10.1038/nature09621.

Koch, B.J., J.F. Ryan, and A.D. Baxevanis. 2012. The diversification of the lim superclass at the base of the metazoa increased subcellular complexity and promoted multicellular specialization. *PLoS One*. 7. doi:10.1371/journal.pone.0033261.

Kong, F., A.J. García, A.P. Mould, M.J. Humphries, and C. Zhu. 2009. Demonstration of catch bonds between an integrin and its ligand. *J. Cell Biol.* 185:1275–1284. doi:10.1083/jcb.200810002.

Le, S., X. Hu, M. Yao, H. Chen, M. Yu, X. Xu, N. Nakazawa, F.M. Margadant, M.P. Sheetz, and J. Yan. 2017. Mechanotransmission and Mechanosensing of Human alpha-Actinin 1. *Cell Rep.* 21:2714–2723. doi:10.1016/j.celrep.2017.11.040.

Lecuit, T., P.F. Lenne, and E. Munro. 2011. Force generation, transmission, and integration during cell and tissue morphogenesis. *Annu. Rev. Cell Dev. Biol.* 27:157–184. doi:10.1146/annurev-cellbio-100109-104027.

Lessey, E.C., C. Guilluy, and K. Burridge. 2012. From mechanical force to RhoA activation. *Biochemistry*. 51:7420–7432. doi:10.1021/bi300758e.

Li, H., K. Huang, L. Gao, L. Wang, Y. Niu, H. Liu, Z. Wang, L. Wang, G. Wang, and J.

Wang. 2016. TES inhibits colorectal cancer progression through activation of p38. *Oncotarget*. 7:45819–45836. doi:10.18632/oncotarget.9961.

Livne, A., E. Bouchbinder, and B. Geiger. 2014. Cell reorientation under cyclic stretching. *Nat. Commun.* 5:1–8. doi:10.1038/ncomms4938.

Ma, H., D. Weng, Y. Chen, W. Huang, K. Pan, H. Wang, J. Sun, Q. Wang, Z. Zhou, H. Wang, and J. Xia. 2010. Extensive analysis of D7S486 in primary gastric cancer supports TESTIN as a candidate tumor suppressor gene. *Mol. Cancer*. 9:1–10.

Oakes, P.W., S. Banerjee, M.C. Marchetti, and M.L. Gardel. 2014. Geometry regulates traction stresses in adherent cells. *Biophys. J.* 107:825–833. doi:10.1016/j.bpj.2014.06.045.

Oakes, P.W., T.C. Bidone, Y. Beckham, A. V. Skeeters, G.R. Ramirez-San Juan, S.P. Winter, G.A. Voth, and M.L. Gardel. 2018. Lamellipodium is a myosin-independent mechanosensor. *Proc. Natl. Acad. Sci. U. S. A.* 115:2646–2651. doi:10.1073/pnas.1715869115.

Oakes, P.W., and M.L. Gardel. 2014. Stressing the limits of focal adhesion mechanosensitivity. *Curr. Opin. Cell Biol.* 30:68–73.

Oakes, P.W., E. Wagner, C.A. Brand, D. Probst, M. Linke, U.S. Schwarz, M. Glotzer, and M.L. Gardel. 2017. Optogenetic control of RhoA reveals zyxin-mediated elasticity of stress fibres. *Nat. Commun.* 8. doi:10.1038/ncomms15817.

Ohashi, K., S. Fujiwara, and K. Mizuno. 2017. Roles of the cytoskeleton, cell adhesion and rho signalling in mechanosensing and mechanotransduction. *J. Biochem.* 161:245–254. doi:10.1093/jb/mvw082.

Oldenburg, J., G. Van Der Krogt, F. Twiss, A. Bongaarts, Y. Habani, J.A. Slotman, A. Houtsmuller, S. Huveneers, and J. De Rooij. 2015. VASP, zyxin and TES are tension-dependent members of Focal Adherens Junctions independent of the α-catenin-vinculin module. *Sci. Rep.* 5:1–14. doi:10.1038/srep17225.

Paluch, E.K., C.M. Nelson, N. Biais, B. Fabry, J. Moeller, B.L. Pruitt, C. Wollnik, G. Kudryasheva, F. Rehfeldt, and W. Federle. 2015. Mechanotransduction : use the force(s). *BMC Biol.* 13:1–14. doi:10.1186/s12915-015-0150-4.

Paszek, M.J., N. Zahir, K.R. Johnson, J.N. Lakins, G.I. Rozenberg, A. Gefen, C.A. Reinhart-

King, S.S. Margulies, M. Dembo, D. Boettiger, D.A. Hammer, and V.M. Weaver. 2005. Tensional homeostasis and the malignant phenotype. *Cancer Cell*. 8:241–254. doi:10.1016/j.ccr.2005.08.010.

Payne-Tobin Jost, A., and J.C. Waters. 2019. Designing a rigorous microscopy experiment: Validating methods and avoiding bias. *J. Cell Biol.* 218:1452–1466. doi:10.1083/jcb.201812109.

Prager-Khoutorsky, M., A. Lichtenstein, R. Krishnan, K. Rajendran, A. Mayo, Z. Kam, B. Geiger, and A.D. Bershadsky. 2011. Fibroblast polarization is a matrix-rigidity-dependent process controlled by focal adhesion mechanosensing. *Nat. Cell Biol.* 13:1457–1465. doi:10.1038/ncb2370.

Rauskolb, C., S. Sun, G. Sun, Y. Pan, and K.D. Irvine. 2014. Cytoskeletal tension inhibits Hippo signaling through an Ajuba-Warts complex. *Cell*. 158:143–156. doi:10.1016/j.cell.2014.05.035.

Ridley, A.J., and A. Hall. 1992. The small GTP-binding protein rho regulates the assembly of focal adhesions and actin stress fibers in response to growth factors. *Cell*. 70:389–399. doi:10.1016/0092-8674(92)90163-7.

Sabass, B., M.L. Gardel, C.M. Waterman, and U.S. Schwarz. 2008. High resolution traction force microscopy based on experimental and computational advances. *Biophys. J.* 94:207–220. doi:10.1529/biophysj.107.113670.

Sala, S., and C. Ampe. 2018. An emerging link between LIM domain proteins and nuclear receptors. *Cell. Mol. Life Sci.* 75:1959–1971. doi:10.1007/s00018-018-2774-3.

Sala, S., M. Catillon, E. Hadzic, E. Schaffner-Reckinger, M. Van Troys, and C. Ampe. 2017a. The PET and LIM1-2 domains of testin contribute to intramolecular and homodimeric interactions. *PLoS One*. 12:1–21. doi:10.1371/journal.pone.0177879.

Sala, S., M. Van Troys, S. Medves, M. Catillon, E. Timmerman, A. Staes, E. Schaffner-Reckinger, K. Gevaert, and C. Ampe. 2017b. Expanding the Interactome of TES by Exploiting TES Modules with Different Subcellular Localizations. *J. Proteome Res.* 16:2054–2071. doi:10.1021/acs.jproteome.7b00034.

Sarti, M., C. Sevignani, G.A. Calin, R. Aqeilan, M. Shimizu, F. Pentimalli, M.C. Picchio, A. Godwin, A. Rosenberg, A. Drusco, M. Negrini, and C.M. Croce. 2005. Adenoviral

transduction of TESTIN gene into breast and uterine cancer cell lines promotes apoptosis and tumor reduction in vivo. *Clin. Cancer Res.* 11:806–813.

Schwarz, U.S., and M.L. Gardel. 2012. United we stand - Integrating the actin cytoskeleton and cell-matrix adhesions in cellular mechanotransduction. *J. Cell Sci.* 125:3051–3060. doi:10.1242/jcs.093716.

Smith, M., L. Hoffman, and M. Beckerle. 2014. LIM Proteins in Actin Cytoskeleton Mechanoresponse. *Trends Cell Biol*. 24:575–583.

Smith, M.A., E. Blankman, N.O. Deakin, L.M. Hoffman, C.C. Jensen, C.E. Turner, and M.C. Beckerle. 2013. LIM Domains Target Actin Regulators Paxillin and Zyxin to Sites of Stress Fiber Strain. *PLoS One*. 8:e69378.

Smith, M.A., E. Blankman, M.L. Gardel, L. Luettjohann, M. Clare, and M.C. Beckerle. 2011. A Zyxin-Mediated Mechanism for Actin Stress Fiber Maintenance and Repair. *Dev Cell*. 19:365–376. doi:10.1016/j.devcel.2010.08.008.A.

Sun, X., D.Y.Z. Phua, L. Axiotakis, M.A. Smith, E. Blankman, R. Gong, R.C. Cail, S. Espinosa de los Reyes, M.C. Beckerle, C.M. Waterman, and G.M. Alushin. 2020. Mechanosensing through Direct Binding of Tensed F-Actin by LIM Domains. *Dev. Cell*. 55:468-482.e7. doi:10.1016/j.devcel.2020.09.022.

Sun, Z., S.S. Guo, and R. Fässler. 2016. Integrin-mediated mechanotransduction. *J Cell Biolournal cell Biol.* 215:445–456.

Suzuki, W., K. Ichikawa, T. Ohki, Y. Kohno, M. Sata, K. Nose, and M. Shibanuma. 2005. Uni-axial stretching regulates intracellular localization of Hic-5 expressed in smooth-muscle cells in vivo. *J. Cell Sci.* 118:937–949.

Svitkina, T. 2018. The actin cytoskeleton and actin-based motility. *Cold Spring Harb. Perspect. Biol.* 10:1–22. doi:10.1101/cshperspect.a018267.

Tatarelli, C., A. Linnenbach, K. Mimori, and C.M. Croce. 2000. Characterization of the human TESTIN gene localized in the FRA7G region at 7q31.2. *Genomics*. 68:1–12. doi:10.1006/geno.2000.6272.

Tobias, E.S., A.F.L. Hurlstone, E. MacKenzie, R. Mcfarlane, and D.M. Black. 2001. The TES gene at 7q31.1 is methylated in tumours and encodes a novel growth-suppressing LIM domain protein. *Oncogene*. 20:2844–2853. doi:10.1038/sj.onc.1204433.

Tojkander, S., G. Gateva, and P. Lappalainen. 2012. Actin stress fibers - Assembly, dynamics and biological roles. *J. Cell Sci.* 125:1855–1864. doi:10.1242/jcs.098087.

Torsoni, A.S., T.M. Marin, L.A. Velloso, and K.G. Franchini. 2005. RhoA/ROCK signaling is critical to FAK activation by cyclic stretch in cardiac myocytes. *Am. J. Physiol. - Hear. Circ. Physiol.* 289:1488–1496. doi:10.1152/ajpheart.00692.2004.

Weeks, R.J., J.L. Ludgate, G. LeMée, and I.M. Morison. 2016. Testin induces rapid death and suppresses proliferation in childhood B acute lymphoblastic leukaemia cells. *PLoS One*. 11:1–19. doi:10.1371/journal.pone.0151341.

Winkelman, J.D., C.A. Anderson, C. Suarez, D.R. Kovar, and M.L. Gardel. 2020. Evolutionarily diverse LIM domain-containing proteins bind stressed actin filaments through a conserved mechanism. *Proc. Natl. Acad. Sci. U. S. A.* 117:25532–25542. doi:10.1073/pnas.2004656117.

Yoshigi, M., L.M. Hoffman, C.C. Jensen, H.J. Yost, and M.C. Beckerle. 2005. Mechanical force mobilizes zyxin from focal adhesions to actin filaments and regulates cytoskeletal reinforcement. *J Cell Biol*. 171:209–215.

Zaidel-Bar, R., S. Itzkovitz, A. Ma'ayan, R. Iyengar, and B. Geiger. 2007. Functional atlas of the integrin adhesome Ronen. *Nat. Cell Biol.* 9:858–867. doi:10.1093/oxfordjournals.bmb.a072535.

Zhu, J., X. Li, X. Kong, M.S. Moran, P. Su, B.G. Haffty, and Q. Yang. 2012. Testin is a tumor suppressor and prognostic marker in breast cancer. *Cancer Sci.* 103:2092–2101. doi:10.1111/cas.12020.

Zimmermann, D., K.E. Homa, G.M. Hocky, L.W. Pollard, E.M. De La Cruz, G.A. Voth, K.M. Trybus, and D.R. Kovar. 2017. Mechanoregulated inhibition of formin facilitates contractile actomyosin ring assembly. *Nat. Commun.* 8:1–12. doi:10.1038/s41467-017-00445-3.

Table S1: Subcellular localization and recruitment magnitude/kinetics of the testin variants used in this study

Testin variant	Subcellular localization	Stress fiber Strain site	Amplitude (fold increase)	Plateau max (fold increase)	$T_{1/2}$ (s)
FL	Cytoplasm/(FA)	/	n/a	n/a	n/a
NT	SF	/	n/a	n/a	n/a
LIM 1-2-3	FA	✓	2.30 +/- 0.12	2.26 +/- 0.06	10.87 +/- 1.83
LIM 1	FA	✓	1.48 +/- 0.09	1.35 +/- 0.05	6.39 +/- 1.33
LIM 2	FA	✓	1.55 +/- 0.12	1.46 +/- 0.09	10.55 +/- 2.31
LIM 3	FA	✓	1.23 +/- 0.11	1.03 +/- 0.04	6.47 +/- 1.30
Y288A	FA	✓	2.20 +/- 6.62	2.42 +/- 6.65	366.76 +/- 1250
Y288E*	FA	✓	1.26 +/- 1.46	1.47 +/- 1.48	285.86 +/- 419
Y288F	Cytoplasm/(FA)	/	n/a	n/a	n/a
Y111A	FA	✓	1.04 +/- 0.10	1.34 +/- 0.10	16.78 +/- 4.97
Y111E	FA	✓	0.92 +/- 0.10	1.13 +/- 0.10	21.99 +/- 5.75
Y111F	Cytoplasm/(FA)	/	n/a	n/a	n/a
E306K	SF/FA	✓	2.59 +/- 1.33	2.84 +/- 1.36	127.63 +/- 88.96
E185K	Cytoplasm/(FA)	✓	0.47 +/- 0.14	0.59 +/- 0.04	4.22 +/- 2.31

*due to the slow kinetics of this construct the fit was based off of traces that were ~4.5 minutes in length compared to ~3 min in length for all other constructs

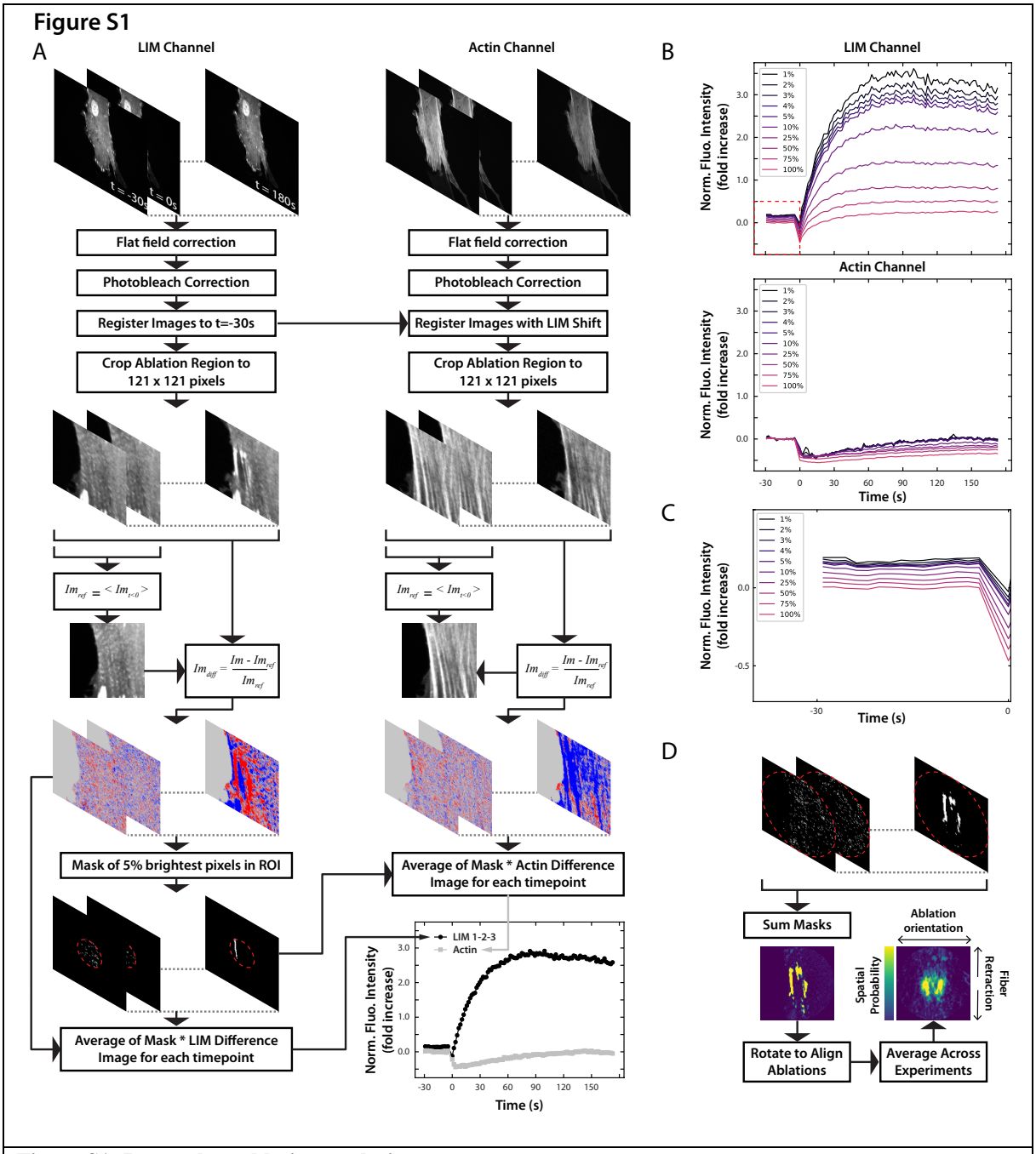

Figure S1: Laser photoablation analysis

A) A graphical representation of the workflow for analyzing the laser ablation and recruitment of testin to SFSSs in Figs. 1-5,7-8. Masks were created based off the testin channel for all experiments (except Figs. 1D,H where zyxin was used instead) and used to calculate the intensity of both the testin and the actin intensities. **B)** The effect of using a different percentage of pixels to create the mask regions causes an offset from zero. **C)** The workflow to calculate the spatial probability maps.

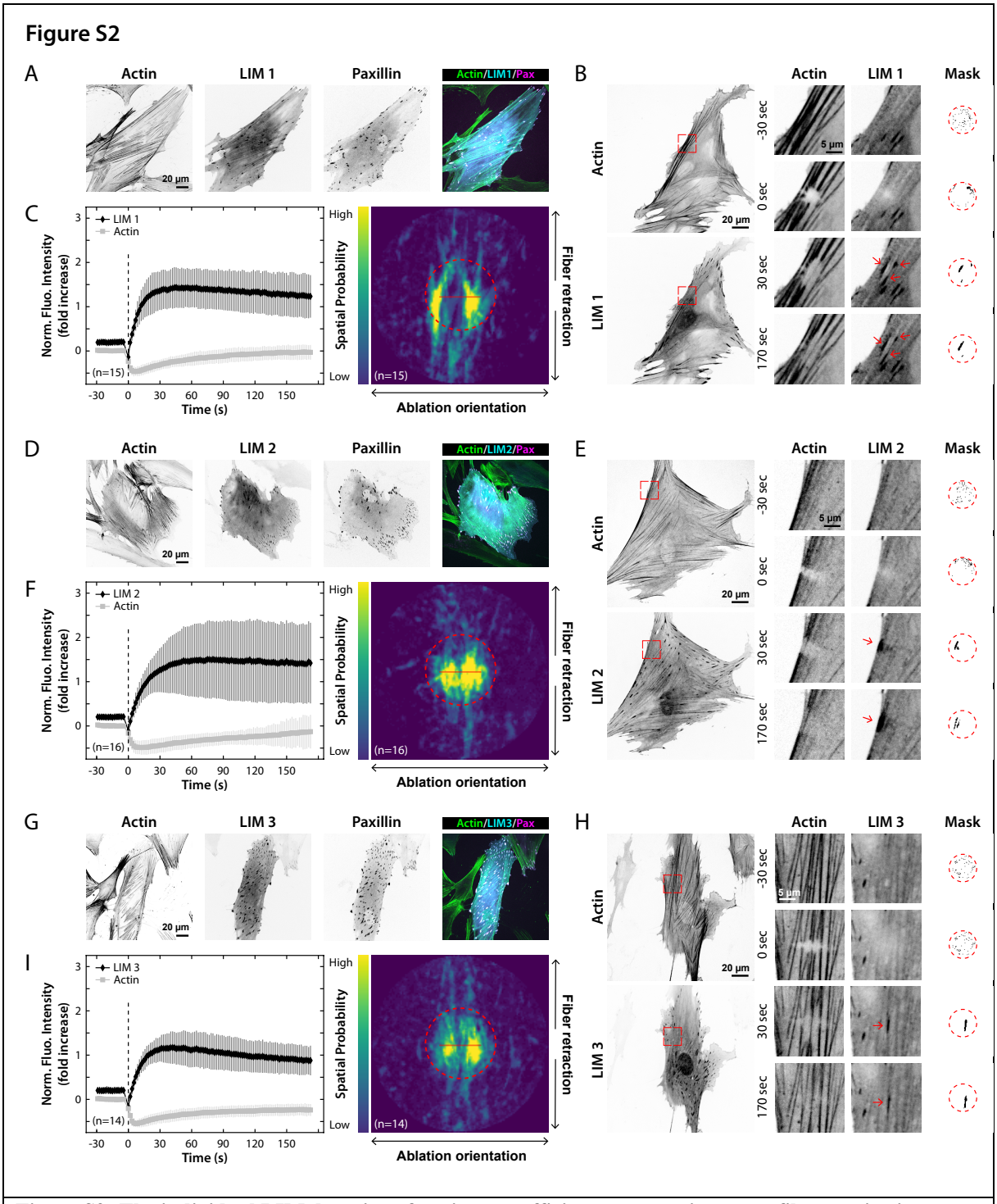

Figure S2: The individual LIM domains of testin are sufficient to recognize stress fiber strain sites
A, D, G) Subcellular localization of the individual LIM domains of testin in HFFs. All LIM domains localize to FAs. GFP-testin, mApple-paxillin and SiR-Actin channels are shown. **B, E, H)** HFFs expressing mApple-actin and GFP-LIM 1 (B) GFP-LIM 2 (E) or GFP-LIM 3 (H). Magnified inset images (red boxed regions) display the localization of each construct during the timelapse demonstrating relocation to SFSSs of each individual LIM domain (red arrows, Movie S3). Mask images show the pixels in the region surrounding the ablation (red dashed circle) that increased the most in intensity compared to their pre-ablation state. **C, F, I)** Average fluorescence intensity traces and standard deviation of the LIM and actin signals (left) and spatial probability of LIM recruitment (right) in the region of strain. Following SFSS induction, a rapid and large increase of all LIM signals was detected in the region of strain (left) and the brightest LIM signals were located in the central region of strain (right, dashed circles). Red line represents the 5 µm laser line used to photo-induce SFSSs.

Figure S3

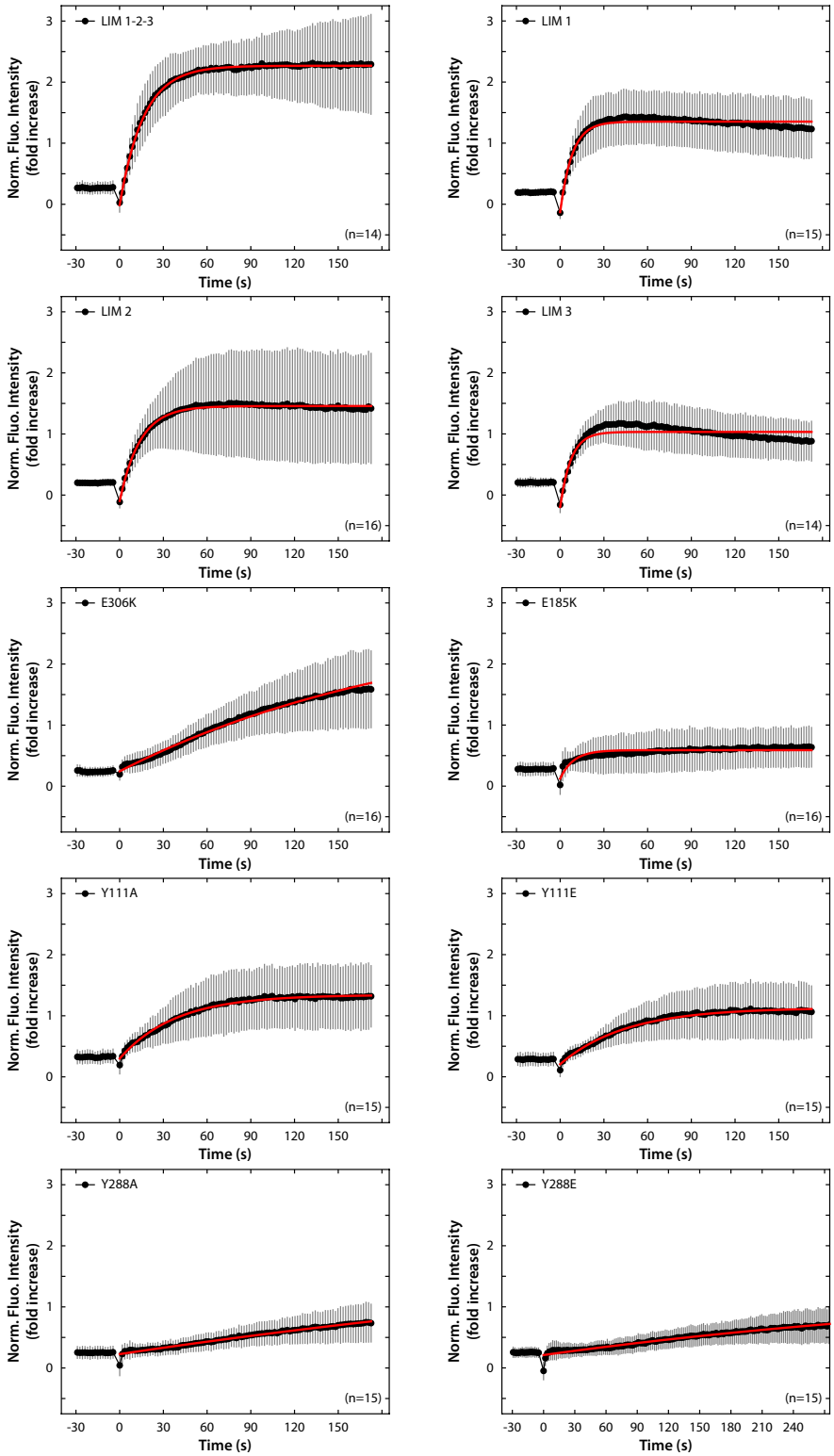

Figure S3: Exponential curve fitting of the average fluorescence intensity traces of mechanosensitive testin variants

Average fluorescence intensity traces are shown for the mechanosensitive testin variants found in this study. The average fluorescence intensity (thick black line) and standard deviation are plotted for each testin variant. An exponential model (red line) with the following equation was used to fit to the average traces: $I(t) = A - Be^{(-t/k)}$ with A: maximum plateau value, B: amplitude, k: time constant. Note that curve fitting for the Y288 mutant is based on a 280-seconds time period for fitting purposes.

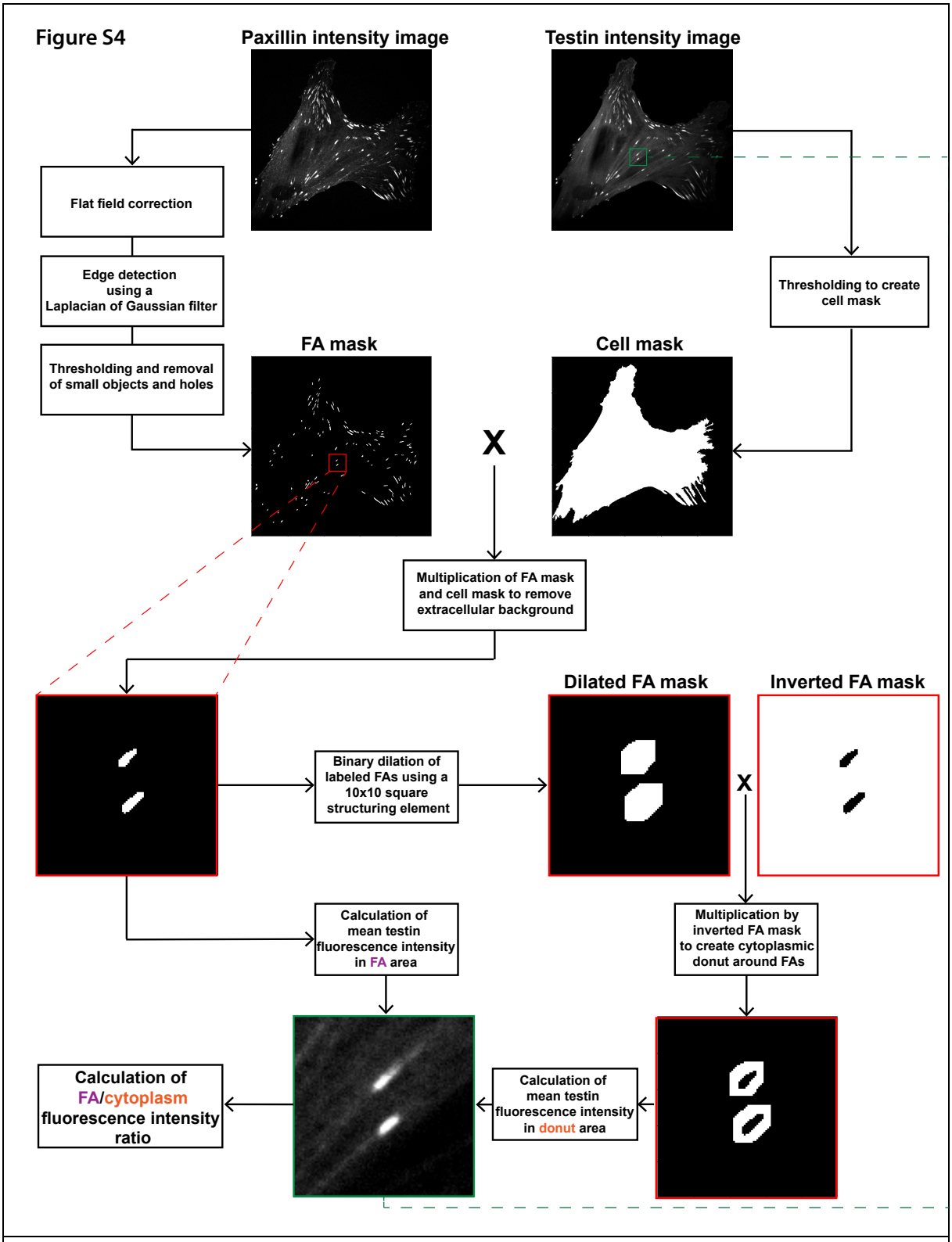

Figure S4: Focal adhesion localization analysis workflow
Each GFP-testin mutant (testin intensity image) investigated in Fig. 4, Fig. 5 and Fig. 7 was co-expressed in HFFs with mApple-paxillin (paxillin intensity image) which was used as an FA marker in the analysis. Flow chart illustrates the different manipulations performed on the input intensity images resulting in the calculation of the ratio of the fluorescence intensity in the FA region and surrounding cytoplasmic region (donut) for a given GFP-testin variant.